

AFGL-TR- 81-0302

12
LEVEL II

AD A108867

A SIMULATION STUDY TO TEST THE PREDICTION OF 1°x 1° MEAN GRAVITY ANOMALIES USING LEAST SQUARES COLLOCATION FROM THE GRAVSAT MISSION

D. P. Hajela

The Ohio State University
Research Foundation
Columbus, Ohio 43212

12 62

September, 1981

Scientific Report No. 9

Approved for public release; distribution unlimited

DTIC FILE COPY

AIR FORCE GEOPHYSICS LABORATORY
AIR FORCE SYSTEMS COMMAND
UNITED STATES AIR FORCE
HANSCOM AFB, MASSACHUSETTS 01731

FW
S D
DTIC
ELECTE
DEC 28 1981
D

ms 400254

8112 28068

Qualified requestors may obtain additional copies from the Defense Technical Information Center. All others should apply to the National Technical Information Service.

UNCLASSIFIED

DG5-316
SCIENTIST

SECURITY CLASSIFICATION OF THIS PAGE (When Data Entered)

REPORT DOCUMENTATION PAGE		READ INSTRUCTIONS BEFORE COMPLETING FORM
1. REPORT NUMBER AFGL-TR-81-0302	2. GOVT ACCESSION NO. AD-A308867	3. RECIPIENT'S CATALOG NUMBER
4. TITLE (and Subtitle) A SIMULATION STUDY TO TEST THE PREDICTION OF 1°x 1° MEAN GRAVITY ANOMALIES USING LEAST SQUARES COLLOCATION FROM THE GRAVSAT MISSION		5. TYPE OF REPORT & PERIOD COVERED Scientific Report No. 9
7. AUTHOR(s) D. P. Hajela		6. PERFORMING ORG. REPORT NUMBER Dept. of Geodetic Sci. 316
9. PERFORMING ORGANIZATION NAME AND ADDRESS The Ohio State University Research Foundation Columbus, Ohio 43210		8. CONTRACT OR GRANT NUMBER(s) F19528-79-C-0027
11. CONTROLLING OFFICE NAME AND ADDRESS Air Force Geophysics Laboratory Hanscom AFB, Massachusetts 01730 Contract Monitor: George Hadgigeorge/LW		10. PROGRAM ELEMENT, PROJECT, TASK AREA & WORK UNIT NUMBERS 61102F 2309G1AW
14. MONITORING AGENCY NAME & ADDRESS (if different from Controlling Office)		12. REPORT DATE September, 1981
		13. NUMBER OF PAGES 52
		15. SECURITY CLASS. (of this report) Unclassified
		15a. DECLASSIFICATION/DOWNGRADING SCHEDULE
16. DISTRIBUTION STATEMENT (of this Report) A - Approved for public release: distribution unlimited		
17. DISTRIBUTION STATEMENT (of the abstract entered in Block 20, if different from Report)		
18. SUPPLEMENTARY NOTES		
19. KEY WORDS (Continue on reverse side if necessary and identify by block number) geodesy, gravity, GRAVSAT		
20. ABSTRACT (Continue on reverse side if necessary and identify by block number) A simulation analysis is described for the determination of an improved gravity field from the GRAVSAT mission by examining the resolution achievable in terms of mean anomaly block size, the accuracy of the predicted anomaly, and testing economical data reduction procedures in terms of computer time. The range-rate ($\dot{\rho}$) data was generated between two low satellites in identical polar orbits at an altitude of 150 km over a		

UNCLASSIFIED

SECURITY CLASSIFICATION OF THIS PAGE (When Data Entered)

spherical earth, with along-track satellite separation of 200 km; and with the anomalous gravitational field being described by 1500 30'x30' anomalies residual to GEM9. The anomalies ($0^\circ \geq \phi \geq 25^\circ\text{S.}$, $130^\circ \leq \lambda \leq 195^\circ\text{E.}$) included those associated with the Tonga Kermadec trench in the south-west Pacific Ocean, and thus provided a severe test of the prediction of the gravitational field. The simulated $\dot{\rho}$ data was impressed with a random noise of 1 $\mu\text{m/s}$.

The noisy $\dot{\rho}$ data was filtered by approximating it by a cubic spline function in the least squares sense and the "line of sight" acceleration, $\ddot{\rho}$, was obtained analytically from the spline function. Mean 1°x1° anomalies (residual to GEM9) were predicted from $\ddot{\rho}$ using least squares collocation after rigorously computing the required covariance function. 30'x30' and 2°x2° anomalies were also predicted to examine the resolution achievable.

Resolution was clearly achieved for anomalies in terms of 1°x1° blocks except when the anomaly gradient varied sharply in the immediate vicinity of the trench, where the "highs" and "lows" in the 1° anomaly field were predicted satisfactorily but the predicted value of intervening 1° anomalies were smoothed out between the extreme values. The very short wavelength variations in the anomaly gradient directly over the trench were not resolvable.

24 predicted 1°x1° anomalies near the trench, but with a comparatively smooth anomaly gradient, agreed with their "true" values with a RMS difference of 5.5 mgals, while the RMS value of true anomalies was 9.5 mgals.

The optimum data configuration, used for predicting a 1°x1° anomaly, was a symmetrical distribution of about 20 data points with a density of 0.4x0.4 in a data cap of radius 1°. The average computer time on Amdahl 470 for predicting a 1° anomaly was 12 seconds, but this will be substantially reduced if the required covariances were interpolated from stored tables instead of rigorous computations used in this study.

UNCLASSIFIED

SECURITY CLASSIFICATION OF THIS PAGE (When Data Entered)

Foreword

This report was prepared by Dr. Dhaneshwar P. Hajela, Associate Professor, Department of Geodetic Science, The Ohio State University, under Air Force Contract No. F19628-79-C-0027, The Ohio State University Research Foundation Project No. 711664, Project Supervisor Richard H. Rapp. The contract covering this research is administered by the Air Force Geophysics Laboratory, Hanscom Air Force Base, Massachusetts, with Mr. George Hadgigeorge, Contract Monitor.

Accession For	
NTIS GRA&I	<input checked="" type="checkbox"/>
DTIC TAB	<input type="checkbox"/>
Unannounced	<input type="checkbox"/>
Justification	
By _____	
Distribution/	
Availability Codes	
Dist	Avail and/or Special
A	

Acknowledgements

I am thankful to Dr. Richard H. Rapp for his suggestions and support of this study, and to Dr. Lem Wong of the Aerospace Corporation for providing and explaining the data tapes. A part of the computer funds was provided by the Instruction and Research Computer Center of the Ohio State University. I also wish to express my appreciation to Miss Susan Carroll for the careful typing of this report.

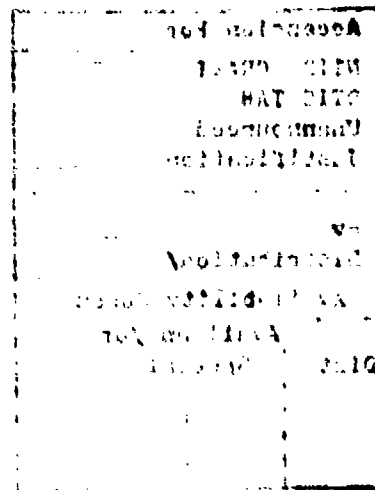


Table of Contents

Foreword	iii
Acknowledgements	v
1. Introduction	1
2. Mathematical Model	2
3. Residual Range Rate Data	6
4. Residual Line of Sight Acceleration.	11
5. Auto- and Cross-Covariance Functions	15
6. Numerical Tests for Data Configuration	27
7. Prediction of $1^\circ \times 1^\circ$ Mean Residual Anomalies. . .	32
8. Prediction of $30' \times 30'$ Mean Residual Anomalies. .	37
9. Prediction of $2^\circ \times 2^\circ$ Mean Residual Anomalies. . .	40
10. Summary and Conclusions	45
References	50

List of Figures

Figure	Title	Page
3.1	A Portion of the Input 30'x 30' Mean Residual Anomalies	7
3.2	Gradient of the Input 30'x 30' Mean Residual Anomalies	8
3.3	Angles Between the Line of Sight and the Axes of the Spherical Coordinate System	10
4.1	Smoothed Residual Range Rate in a Central S/N Arc	13
4.2	Residual Line of Sight Acceleration for the Arc in Fig. 4.1	14
5.1	Covariance Function of the Line of Sight Acceleration	17
5.2	Cross-Covariance Function Between Surface Gravity Anomaly and Line of Sight Acceleration	19
5.3	Data Selection for Predicting Anomaly Block and Comparison of Data Points for N/S and S/N Arcs	20
5.4	Residual Range Rate Data in (a) N/S, (b) S/N Arcs	22,23
5.5	Residual Line of Sight Acceleration in (a) N/S, (b) S/N Arcs	24,25
5.6	Estimator or Weighting Function for 1°x 1° Mean Residual Anomalies from Residual Line of Sight Accelerations	26
6.1	1°x 1° Mean Residual Anomalies	28
6.2	Gradient of the 1°x 1° Mean Residual Anomalies	29
7.1	Prediction of 1°x 1° Mean Residual Anomalies	36
8.1	Prediction of 30'x 30' Mean Residual Anomalies	39

9.1	2°x 2° Mean Residual Anomalies	41
9.2	Gradient of the 2°x 2° Mean Residual Anomalies	42
9.3	Prediction of 2°x 2° Mean Residual Anomalies	43

List of Tables

Table	Title	Page
4.1	Filtering of Noise in $\dot{\rho}$ for Different Spline Knot Spacing	12
6.1	Variation in the Predicted 1° Anomaly with Variation in Extent (ψ°) of $\dot{\rho}$ Data	31
6.2	Variation in the Predicted 1° Anomaly with Variation in Density of $\dot{\rho}$ Data	31
7.1	Prediction of 1° Anomalies in Area 8° to 12°S., 184° to 190°E.	34
7.2	Prediction of 1° Anomalies in Area 12° to 16°S., 186° to 188°E.	35
8.1	Prediction of 30' Anomalies in Area 8° to 12°S., 186° to 188°E.	38
9.1	Prediction of 2° Anomalies in Area 8° to 18°S., 184° to 190°E.	44

1. Introduction

The report on "Applications of a Dedicated Gravitational Satellite Mission" (National Academy of Sciences, 1979) recommended rigorous simulation analyses to answer questions on the resolution, accuracy, economical data reduction procedures, etc., for an improved gravity field from the GRAVSAT mission.

Several error analyses have been reported recently for both the "High-Low" and "Low-Low" missions. Pisacane and Yionoulis (1980), and Douglas et al. (1980) used least squares "deterministic" techniques to get estimate of $1^\circ \times 1^\circ$ anomaly recovery errors. Lancaster et al. (1980) used similar techniques but obtained less optimistic estimates. Least squares collocation techniques were applied by Rapp and Hajela (1979) for the "High-Low" case, and by Rummel (1980) for the "Low-Low" case. Krynski (1979) also used the collocation method for his error analysis. Jekeli and Rapp (1980), Breakwell (1980), Breakwell and Duhamel (1981) related the spectrum of the measurement of range-rate and gradiometry to the spectrum of the disturbing potential of the earth's gravity field to get better insight into resolution and achievable accuracies.

These error analyses have helped to define the current GRAVSAT mission configuration plan (Bergeson-Willis et al., 1981) of two low satellites at an altitude of 160 km, in the same polar orbit but separated by 300 km. The uncertainty of relative range-rate measurement is expected to be less than $1 \mu\text{m/s}$. Wong and Sjogren (1980) describe the simulation of range-rate data from 1500 $30' \times 30'$ mean anomalies residual to GEM9 (Lerch et al., 1979) for a configuration closely corresponding to the current GRAVSAT configuration. The anomalies are in and around the sharply varying field associated with the Tonga Kermadec Trench in the south-west Pacific Ocean. This data is described in Section 3 and will be used in the present simulation study.

The least squares collocation method is used, described in Section 2, to predict the $30' \times 30'$, $1^\circ \times 1^\circ$ and $2^\circ \times 2^\circ$ residual anomalies. The predicted anomalies are compared with the input anomalies used for generating the data. The purpose of the present study is thus to test the prediction of gravity anomalies from the GRAVSAT mission, to draw conclusions for the data requirement for economical (in terms of computer time) prediction, and to establish the resolution achievable in terms of the block size of the mean anomalies.

The computation of line of sight accelerations sensed at the satellite altitude is described in Section 4. The computation of the covariances needed in the collocation method is discussed in Section 5 while the tests for the

effect of the extent and density of data on the predicted anomaly are discussed in Section 6. The numerical results with the resulting modest data requirement in terms of computer time are discussed in Section 7 for the prediction of 1° anomalies. The resolution achievable in terms of anomaly block size is discussed in Sections 8 and 9 by considering the prediction of 30' and 3° anomalies respectively. A representative sample of anomalies is chosen in a comparatively smooth area away from but near the trench, and the sample is then extended to include anomalies in the area approaching and then directly over the trench.

2. Mathematical Model

We define the residual range-rate $\dot{\rho}$ between the two satellites in the earth's anomalous potential field T

$$(2.1) \quad \dot{\rho} = \dot{\rho}_0 - \dot{\rho}_c$$

$$(2.2) \quad T = V - U$$

where $\dot{\rho}_0$ is the range-rate in the earth's gravitational potential field V and $\dot{\rho}_c$ is the range-rate in the earth's normal potential field U, which was taken in this study to be described by GEM9.

It is easily seen that

$$(2.3) \quad \dot{\rho}_0 = \dot{\underline{x}}_{12} \cdot \underline{e}_{12}, \quad \dot{\underline{x}}_{12} = \dot{\underline{x}}_2 - \dot{\underline{x}}_1$$

where \underline{x} , $\dot{\underline{x}}$ are the position and velocity vectors of the satellites in a geocentric quasi-inertial cartesian coordinate system; subscripts 1 and 2 refer to the lead and trailing satellites respectively e.g. in a north to south arc or vice versa; and \underline{e}_{12} is the unit line of sight vector from the lead to the trailing satellite. We assume that the range-rate is measured at the lead satellite. Equation (2.3) expresses the fact that the range-rate is the projection of the relative velocity of the satellites on the line of sight between the satellites.

The time-derivative of the range-rate, which we may call as line of sight acceleration, is obtained from (2.3) as:

$$(2.4) \quad \ddot{\rho}_0 = \ddot{\underline{x}}_{12} \cdot \underline{e}_{12} + \dot{\underline{x}}_{12} \cdot \dot{\underline{e}}_{12}$$

and we define the residual line of sight acceleration $\ddot{\rho}$

analogously to (2.1) as:

$$(2.5) \quad \ddot{\rho} = \ddot{\rho}_0 - \ddot{\rho}_c$$

Rummel (1980, p.5, Table 1) has shown that the second term in equation (2.4) is negligibly small as compared to the first term when applied for the residual line of sight acceleration $\ddot{\rho}$, and we may write with a negligibly small error (ibid., p.11)

$$(2.6) \quad \ddot{\rho} \approx \underline{\ddot{x}}_{12} \cdot \underline{e}_{12} = (\underline{\ddot{x}}_2 - \underline{\ddot{x}}_1) \cdot \underline{e}_{12} = (\underline{\nabla T}_2 - \underline{\nabla T}_1) \cdot \underline{e}_{12}$$

where $\underline{\nabla T}$ is the gradient of the anomalous potential at the satellite location. Again, the assumption in (2.6) is that $\ddot{\rho}$ is sensed at the location of lead satellite analogously to the measurement of range-rate at that location in (2.3).

We will henceforward treat $\ddot{\rho}$ as the "observation" related to the anomalous potential at satellite location through (2.6). The reduction of $\ddot{\rho}$ from $\dot{\rho}$ will be described in Section 4.

We may denote $\underline{\nabla T}$ in terms of its components $\delta_r, \delta_{\phi'}, \delta_{\lambda}$ in a geocentric earth-fixed spherical coordinate (r, ϕ', λ) system. Then following Heiskanen and Moritz (1967, Section 6-4), we have:

$$(2.7) \quad \underline{\nabla T} = \delta_r \underline{e}_r + \delta_{\phi'} \underline{e}_{\phi'} + \delta_{\lambda} \underline{e}_{\lambda}$$

$$\text{where } \delta_r = \partial T / \partial r$$

$$\delta_{\phi'} = (1/r) (\partial T / \partial \phi') = -\gamma \xi$$

$$\delta_{\lambda} = (1/r \cos \phi') (\partial T / \partial \lambda) = -\gamma \eta$$

where γ is the normal gravity at the satellite location and ξ, η are the latitudinal and meridional components of the deflection of vertical at the satellite location.

We use a_1, b_1, c_1 to denote the direction cosines of line of sight (lead satellite 1 to trailing satellite 2) with r, ϕ', λ axes at location of lead satellite; and similarly a_2, b_2, c_2 as direction cosines of line of sight (trailing satellite 2 to lead satellite 1) with r, ϕ', λ axes at location of trailing satellite. Then by inserting (2.7) into (2.6), we get:

$$(2.8) \quad \begin{aligned} \ddot{\rho} &= (\underline{\nabla T}_2 - \underline{\nabla T}_1) \cdot \underline{e}_{12} = -\underline{\nabla T}_2 \cdot \underline{e}_{21} - \underline{\nabla T}_1 \cdot \underline{e}_{12} \\ &= -a_2 \delta_{r2} + b_2 \gamma_2 \xi_2 + c_2 \gamma_2 \eta_2 - a_1 \delta_{r1} + b_1 \gamma_1 \xi_1 + c_1 \gamma_1 \eta_1 \end{aligned}$$

The direction cosines a , b , c of the line of sight may be rigorously computed by relating the geocentric cartesian and spherical coordinates of the satellites, e.g. see Hajela (1979, equations (10) to (13)). For the simple configuration of satellites in this simulation study, the direction cosines may also be obtained from simple geometric considerations (see Section 3).

The predicted value $\hat{\Delta g}'$ of a mean residual gravity anomaly is obtained from $\hat{p} \equiv T_\ell$ (for ease of notation) "observations" by least squares collocation (Moritz, 1980, Section 14):

$$(2.9) \quad \hat{\Delta g}' = \underline{C}_{\Delta g', T_\ell}^T \underline{C}^{*-1} T_\ell, \quad \underline{C}^* = \underline{C}_{T_\ell, T_\ell} + \underline{D} \\ = \underline{A} T_\ell$$

where $\underline{C}_{T_\ell, T_\ell} \equiv \text{cov}(T_\ell, T_\ell)$ is the covariance matrix of residual accelerations $\hat{p} \equiv T_\ell$; $\underline{D} = \sigma_{T_\ell}^2 \underline{I}$ is noise matrix of T_ℓ , taken as a diagonal matrix with equal variance ($\sigma_{T_\ell}^2$) of T_ℓ data on the diagonal (see Section 4); $\underline{C}_{\Delta g', T_\ell} \equiv \text{cov}(\Delta g', T_\ell)$ is the covariance vector of T_ℓ with the predicted mean anomaly block, and the superscript T is for the transpose. The covariance with the mean block is obtained by numerical integration of the point covariances after dividing the block into $m \times m$ sub-blocks. By numerical tests, it was found that $m=4, 5, 6$ is adequate for $30'$, 1° and 2° blocks. The estimating operator \underline{A} and the underlying covariances $\text{cov}(T_\ell, T_\ell)$ and $\text{cov}(\Delta g', T_\ell)$ will be discussed in Section 5.

The residual anomaly $\Delta g'$ is obtained from anomaly Δg , referred to an ellipsoidal field, by subtracting the anomaly Δg_U implied by the normal potential U , e.g. see Rummel et al. (1976, p.20).

The estimate of the variance $\hat{\sigma}^2_{\Delta g'}$ of the predicted residual anomaly is given by:

$$(2.10) \quad \hat{\sigma}^2_{\Delta g'} = C_0 - \underline{C}_{\Delta g', T_\ell}^T \underline{C}^{*-1} \underline{C}_{\Delta g', T_\ell}$$

where C_0 is the variance of the residual anomalies of specified block size and is dependent on its latitude in the case of equi-angular blocks.

The covariances needed in (2.9) and (2.10) are computed by the propagation of covariances utilizing (2.8). For example, for the data points i and j ; $i=1, \dots, n$, $j=1, \dots, i$; the corresponding element in the matrix $\underline{C}_{T_\ell, T_\ell}$ is obtained by:

$$\begin{array}{l}
 (2.11) \\
 \text{cov}(T_{\ell i}, T_{\ell j}) \\
 \equiv (T_{\ell i}, T_{\ell j})
 \end{array}
 \begin{array}{c}
 \delta_{rj2} \quad \xi_{j2} \quad \eta_{j2} \quad \delta_{rj1} \quad \xi_{j1} \quad \eta_{j1} \\
 \left[\begin{array}{ccc}
 (\delta_{ri2}, \delta_{rj2}) & \cdot & \cdot & \cdot & (\delta_{ri2}, \eta_{j1}) \\
 (\xi_{i2}, \delta_{rj2}) & \cdot & \cdot & \cdot & (\xi_{i2}, \eta_{j1}) \\
 (\eta_{i2}, \delta_{rj2}) & \cdot & \cdot & \cdot & (\eta_{i2}, \eta_{j1}) \\
 (\delta_{ri1}, \delta_{rj2}) & \cdot & \cdot & \cdot & (\delta_{ri1}, \eta_{j1}) \\
 (\xi_{i1}, \delta_{rj2}) & \cdot & \cdot & \cdot & (\xi_{i1}, \eta_{j1}) \\
 (\eta_{i1}, \delta_{rj2}) & \cdot & \cdot & \cdot & (\eta_{i1}, \eta_{j1})
 \end{array} \right]
 \begin{array}{c}
 -a_{j2} \\
 b_{j2} \gamma_{j2} \\
 c_{j2} \gamma_{j2} \\
 -a_{j1} \\
 b_{j1} \gamma_{j1} \\
 c_{j1} \gamma_{j1}
 \end{array}
 \end{array}$$

$$= [-a_{12}, b_{12} \gamma_{12}, c_{12} \gamma_{12}, -a_{11}, b_{11} \gamma_{11}, c_{11} \gamma_{11}] \cdot$$

Similarly, a point covariance between $T_{\ell i}$ and $\Delta g'$, say at the center c' anomaly block is given by:

$$\begin{array}{l}
 (2.12) \\
 \text{cov}(T_{\ell i}, \Delta g') \\
 \equiv (T_{\ell i}, \Delta g')
 \end{array}
 \begin{array}{c}
 \left[\begin{array}{c}
 (\delta_{ri2}, \Delta g') \\
 (\xi_{i2}, \Delta g') \\
 (\eta_{i2}, \Delta g') \\
 (\delta_{ri1}, \Delta g') \\
 (\xi_{i1}, \Delta g') \\
 (\eta_{i1}, \Delta g')
 \end{array} \right]
 \end{array}$$

$$= [-a_{12}, b_{12} \gamma_{12}, c_{12} \gamma_{12}, -a_{11}, b_{11} \gamma_{11}, c_{11} \gamma_{11}] \cdot$$

The computation of (2.11) and (2.12) is discussed further in Section 5. Some simplification also results due to similar values of some direction cosines in this simulation study. The auto- and cross-covariances of δ_r , ξ , η , $\Delta g'$ are computed from subroutine COVAX (Tscherning, 1976) after modifying it to give all required covariances in mgals² to correspond to the units of $(T_{\ell i}, T_{\ell j})$ and $(T_{\ell i}, \Delta g')$. The degree variances for $\ell = 3, \dots, 20$ were made zero as we are considering residual accelerations $\ddot{\rho} \equiv T_{\ell}$ and anomalies residual to GEM9, which is complete to degree and order 20. Though the low degree variances in GEM9 and the model are strictly not the same, this approximation has negligibly small effect on equations (2.3) and (2.10). The underlying anomaly degree variance (c_{ℓ}) model used is (see Tscherning and Rapp, 1974):

$$(2.13) \quad c_{\ell} = \frac{425.28(\ell - 1)}{(\ell - 2)(\ell + 24)} \text{ mgals}^2 ; \quad r_B = 6,369,779.8 \text{ m} ,$$

where r_B is the radius of the Bjerhammar sphere internal to the earth's surface, so that the degree variance $\sigma_l(\Delta g)$ at a point with geocentric distance r is given by:

$$(2.14) \sigma_l(\Delta g) = s^{l+2} c_l ; s = (r_B/r)^2 .$$

3. Residual Range Rate Data

Wong and Sjogren (1980, Sec.2.2) simulate the range rate between two low satellites at an altitude of 150 km above a spherical earth. The two satellites were in the same polar orbit, i.e. same geocentric longitude for both satellites for any range rate measurement, with a separation of 200 km = $1:7554\dots$ between the two satellites. The satellite ephemeris was perturbed by the anomalous gravity field defined by 1500 30' x 30' anomalies covering the area bounded by latitudes 0° to 25° S. and longitudes 180° to 195° E. These anomalies were obtained from altimeter measurements (R.H. Rapp, private communication, 1980), and from these the anomaly implied by GEM9 was subtracted out. Accordingly, the simulated measurement corresponded to residual range rate $\dot{\rho}$ in (2.1).

A random noise (mean = 0 , $\sigma = 1\mu\text{m/s}$) was impressed on $\dot{\rho}$ to simulate the precision of the GRAVSAT mission. The integration time and the data interval along an arc was 2 seconds ($\Delta\phi = 0:14$), while the separation between arcs in longitude, $\Delta\lambda$, was 0:2 in the central half of the area and 0.4° in longitude on each side. This density of arcs was obtained for both N/S (lead satellite moving from north to south) and S/N (lead satellite moving from south to north) arcs. A total of 23,128 "noisy" $\dot{\rho}$ measurements were generated over 59 each N/S and S/N arcs, and sent to us on a magnetic tape for this study (L. Wong, private communication, 1980).

A portion of the input 30' residual anomalies are shown in Figure 3.1. These have been contoured at 20 mgals interval in Figure 3.2 to show the gradient of the anomaly field. We notice that the field is comparatively smooth from the north edge up to 12° S., varies sharply as the trench is approached around 14° S. from where the trench proceeds south generally about the longitude 187:5 E. The area for testing the prediction of 1°x 1° anomalies was accordingly selected between 8° to 16° S. and 186° to 188° E. (and slightly to east and west) astride the steep gradients of the trench, and also covering a comparatively smoother field in the northern portion. The 1° anomalies, (which were predicted based on $\dot{\rho}$ generated from the input 30' anomalies,) reflect the general gradient of the 30' anomalies. The 1° anomaly field will be discussed in Sections 6 and 7.

The $\dot{\rho}$ measurements on the data tape were identified with time along the arc from specified starting position of

-4	-8	-12	-10	-10	2	6	-3	-15	-2	3	7	17	8	18	-12	-2	-2	-10	1	-1
	-1	-2	0	-3	5	5	-8	-5	-18	-14	9	23	22	16	-7	0	5	-21	-12	-3
	5	-5	-10	-8	-8	-12	-12	11	-12	-15	-8	-1	-10	-18	-12	-8	3	-3	-2	3
	-5	-7	-5	-10	-20	-27	-1	11	-4	-16	-20	-5	-4	-15	-12	-20	-21	13	8	4
-6	-8	-6	-10	-15	-19	-20	-2	4	-2	-17	-16	-1	0	-12	-12	-21	-20	-1	-7	-8
	-10	-10	-18	-26	-29	-16	-11	-7	-5	-15	-17	-7	-3	-5	-6	-9	-9	-4	-5	-7
	-8	-13	-17	-27	-15	-3	-17	-3	4	-13	-22	-13	-4	-5	-13	-16	-11	-3	-3	-5
	-6	-14	-16	-15	-0	-16	-26	-12	-2	-13	-23	-16	-3	-4	-13	-19	-7	-1	-2	-1
-8	2	-3	-20	-11	5	-14	-20	-16	-15	-13	-7	-8	-5	-8	-13	-8	3	-6	-7	-4
	-4	-7	-26	0	10	-12	-10	-19	-19	3	13	-1	-13	-14	-9	3	-5	-11	-12	-24
	-18	-22	-6	3	-21	-21	-8	-5	-6	10	20	4	8	6	-5	4	-8	-10	-8	-25
	-26	-15	1	-3	-14	-12	-3	4	7	12	23	-5	-13	2	-10	-6	2	13	-10	-5
-10	-31	-5	2	-8	-3	2	2	-2	5	9	17	11	-4	-3	-12	-5	3	2	-6	22
	-31	-5	-5	-4	-5	-3	-2	-8	-2	3	-0	16	16	-2	-8	2	4	-18	-1	15
	-10	-7	-15	-18	-10	-18	-28	-17	-10	-10	-13	13	19	6	-1	3	2	-19	-8	-2
	18	2	-16	-24	-10	-25	-24	-7	-6	-30	-12	-2	3	10	6	8	-17	-8	-9	-8
-12	-4	6	4	-8	-11	-12	10	38	9	-32	-31	-21	-15	13	11	-8	-14	-8	3	-0
	-16	-23	-5	-1	-10	-18	5	25	-26	-42	-18	-21	-21	-8	-0	-28	-9	-2	2	-3
	-28	-32	-19	1	-3	-12	3	-4	-36	-8	49	44	8	-18	-19	-17	3	-2	-7	-10
	16	-6	-1	-25	-42	-25	-9	-23	-30	-4	57	54	16	-4	-12	28	57	21	-8	-12
-14	24	10	22	1	-38	-27	-18	-18	-32	-42	-5	8	8	20	42	67	105	57	4	-12
	-2	8	17	25	8	-0	11	16	1	-100	-88	-32	-19	14	32	38	55	28	-7	-6
	-16	0	11	21	15	12	24	47	85	-12	-82	-107	-44	-0	11	4	8	-10	-28	-7
	-3	-3	6	11	9	11	28	47	80	70	-55	-141	-74	-5	37	17	-10	-19	-15	0
-16	-2	-5	-3	3	6	14	30	51	77	67	-45	-163	-81	3	51	28	-8	-8	5	7
	-5	-7	-3	1	8	24	34	55	71	49	-51	-150	-78	15	39	28	3	0	15	11
	2	-3	-6	-8	17	27	40	65	80	52	-85	-143	-38	25	16	10	13	10	15	11
	-7	4	-5	-3	20	31	47	76	86	81	-68	-141	-12	33	14	-6	11	20	15	15
-18	2	7	-5	8	20	33	56	84	79	18	-118	-110	-7	23	17	7	20	35	24	7
	-3	-8	13	16	21	36	67	118	68	-71	-130	-78	-8	15	11	21	48	37	18	2
	-12	-9	21	22	30	50	78	127	49	-122	-143	-71	-11	14	13	43	88	14	3	8
-20	-10	-1	18	28	40	70	116	122	8	-148	-153	-88	-4	16	17	20	7	-8	-2	10
	182	183	184	185	186	187	188	189	190	191	192									

Figure 3.1 A Portion of the Input 30'x 30' Mean Residual (to GEM9) Anomalies in mgals. 1500 anomalies covering $0^\circ \leq \phi \leq 25^\circ$ S., $180^\circ \leq \lambda \leq 195^\circ$ E. were used to simulate δ data.

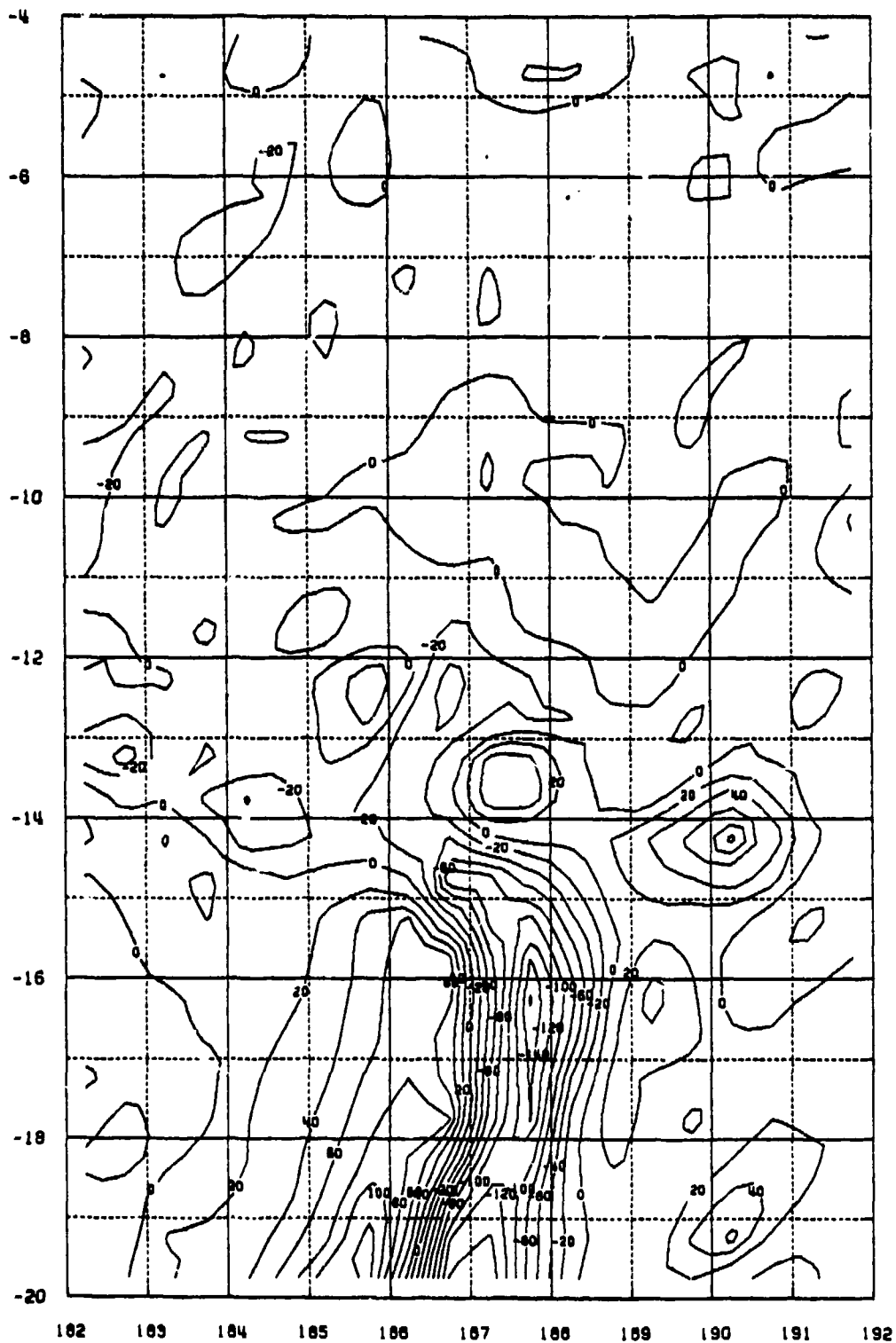


Figure 3.2 Gradient of the Input 30'x 30' Mean Residual
(to GEM9) Anomalies. Contour Interval 20 mgals.

the lead (and trailing satellite) but the actual location of the satellites for a particular ρ was not given, except for sample runs for one N/S and S/N arc at intervals of 30 seconds. The geocentric spherical coordinates (r, ϕ', λ) of the satellites were computed by us in the following simple manner and agreed with the sample values to about 0:004 and 0:001 in latitude and longitude respectively. As the satellite orbits were generated over a spherical earth, the period P of the satellite is given by

$$(3.1) \quad P = 2\pi a^{3/2} / (GM)^{1/2}, \quad a = a_e + 150 \text{ km}$$

≈ 5249 s for the specified values of earth radius a_e and the gravitational constant times earth's mass GM .

Further, as the satellites are in a circular orbit and the inertial starting azimuth is 180° or 0° for N/S and S/N arcs respectively, the change in declination ($\Delta\delta$) or geocentric latitude ($\Delta\phi'$) was constant over short arc span of about $6\frac{1}{2}$ minutes; and we have for the data interval of 2 seconds:

$$(3.2) \quad \Delta\phi' = \Delta\delta = \frac{360^\circ}{P} \cdot 2 \quad \text{with } \Delta\phi' \text{ in degrees and } P \text{ in seconds.}$$

The geocentric longitude of the satellite changes only due to the rotation of the earth, and finally the height h above the ellipsoid may be calculated from:

$$(3.3) \quad h = a - \rho, \quad \rho = a(1 - e^2)^{1/2} / (1 - e^2 \cos^2 \phi')^{1/2}$$

Here ρ is the radius vector to the ellipsoid at geocentric latitude ϕ' , and e is the first eccentricity. However, as the satellite orbits were generated over a spherical earth, h was uniformly taken as 150 km.

The direction cosines in equation (2.8, of the line of sight with the (r, ϕ', λ) axes at the two satellites ($k=1,2$) for different ρ (and $\dot{\rho}$) data points ($i=1, \dots, n$) can be simply obtained from geometric considerations because of the simple configuration of satellites. This is shown in Figures 3.3a and 3.3b, where two data points $i, i+1$ have been considered for a N/S and a S/N arc respectively. As the two satellites are in a circular orbit the line of sight ℓ_{ik} makes equal angles with the radial direction at $k=1,2$ for all i , and this is a constant angle because of constant separation between the satellites of 200 km ($\theta = 1:7554 \dots = 1^\circ 45' 19''$). Also the longitude of the two satellites is the same for all i . Accordingly, the angles $\alpha_{ik}, \beta_{ik}, \gamma_{ik}$ of ℓ_{ik} with the positive direction of axes, and thus the direction cosines a_{ik}, b_{ik}, c_{ik} are as follows:

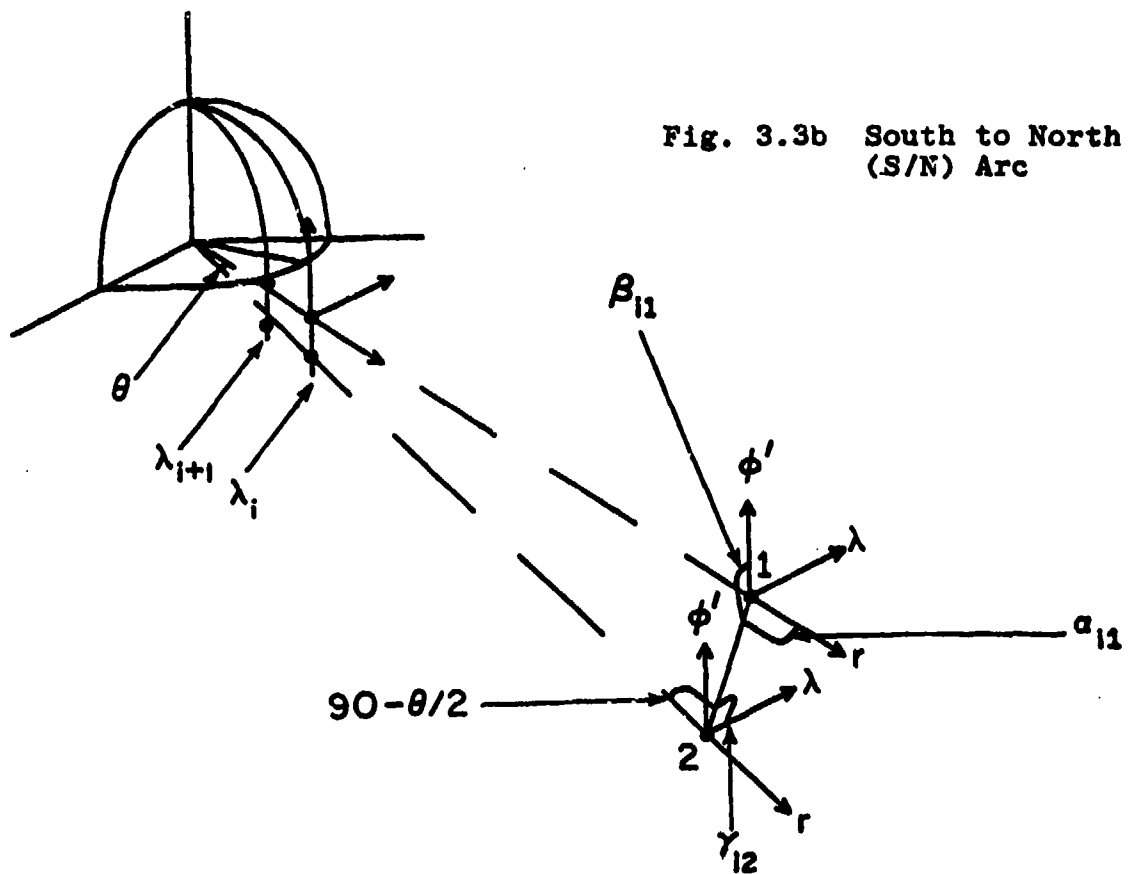
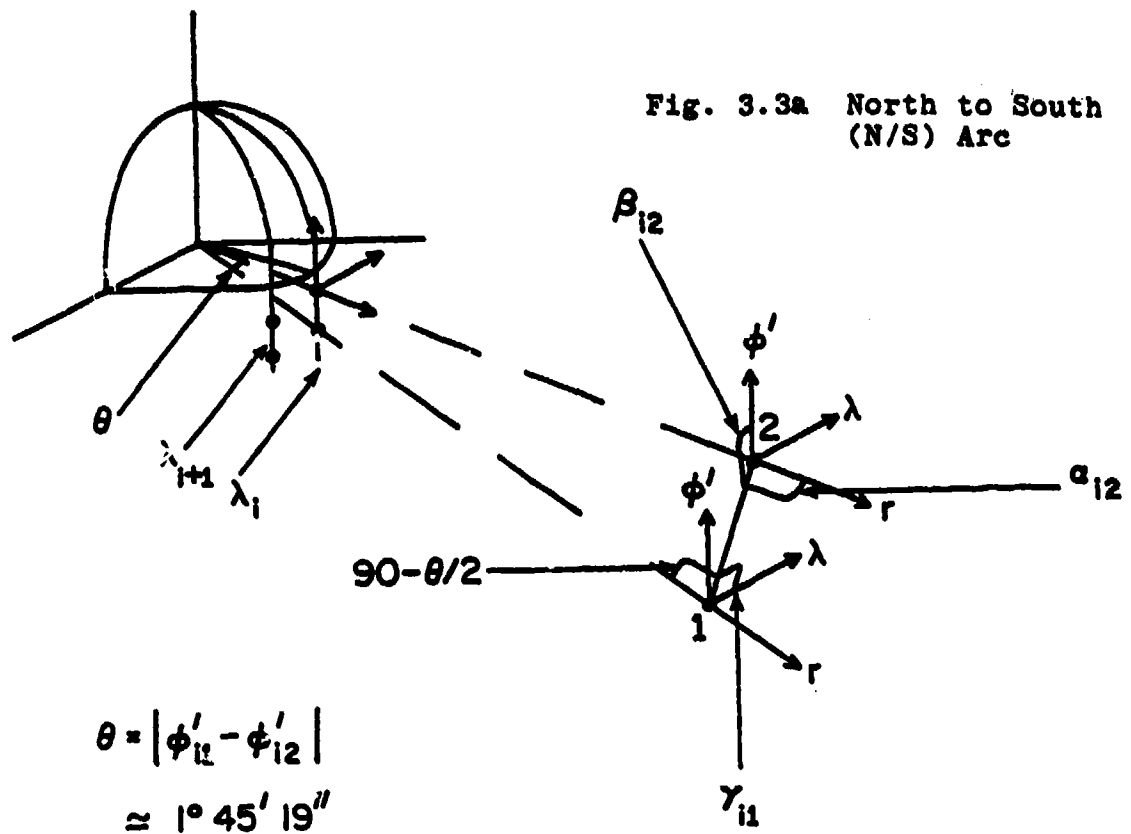


Figure 3.3 Angles Between the Line of Sight and the Axes of the Spherical Coordinate System

$$\begin{aligned}
\alpha_{ik} &= 90^\circ 52' 40'' \quad , \text{ for } k=1,2, \text{ for all } i; \text{ for all N/S and S/N arcs} \\
a_{ik} &= (l_{ik}, r_k) = -0.015, 318... \\
\beta_{ik} &= 0^\circ 52' 40'' \quad , \text{ for } k=1; \text{ for all } i; \text{ for all N/S arcs} \\
&\quad \text{and for } k=2; \text{ for all } i; \text{ for all S/N arcs} \\
(3.4) \quad \beta_{ik} &= 180^\circ 52' 40'' \quad , \text{ for } k=2; \text{ for all } i; \text{ for all N/S arcs} \\
&\quad \text{and for } k=1; \text{ for all } i; \text{ for all S/N arcs} \\
b_{ik} &= (l_{ik}, \phi'_k) = \pm 0.999, 882... \\
\gamma_{ik} &= 90^\circ \quad , \text{ for } k=1,2; \text{ for all } i; \text{ for all N/S and S/N arcs} \\
c_{ik} &= (l_{ik}, \lambda_k) = 0
\end{aligned}$$

4. Residual Line of Sight Acceleration

The simulated residual range rate $\dot{\rho}$ was first filtered for the "observational" noise of $1 \mu\text{m/s}$ by approximating the $\dot{\rho}$ values in the least squares sense with a cubic spline function ($\dot{\rho}_s$) with fixed knots (see Hajela, 1979, equations (17) to (19)). The spline function $\dot{\rho}_s$ was then differentiated to get $\ddot{\rho}$. The degree of smoothing or the filtering of noise depends on the spacing of the spline knots; a larger spacing results in a greater smoothing. Several different knot spacing were tested at 4, 6, 8, 10, 12, 14, 16 seconds for a maximum of 121 $\dot{\rho}$ data points at 2 seconds interval in several N/S and S/N arcs. The difference, $\Delta\dot{\rho}$, between the smoothed spline function $\dot{\rho}_s$ and the noisy $\dot{\rho}$ data was examined after discarding the data points in two intervals each in the beginning and the end of the approximating spline function. This was done to discard the data affected by spurious oscillations in the spline because of arbitrary end conditions.

$$(4.1) \quad \Delta\dot{\rho} = \dot{\rho}_s - \dot{\rho}$$

Some statistics for one N/S and one S/N arc in the center of the area are given in Table 4.1.

Table 4.1 Filtering of Noise in $\dot{\rho}$ for Different Spline Knot Spacing

SPLINE KNOT SPACING (sec.)	# PTS.	RMS VALUE		STATISTICS FOR $\Delta\dot{\rho}$ ($\mu\text{m/s}$)			
		$\dot{\rho}$ ($\mu\text{m/s}$)	$\dot{\rho}_s$	MEAN	RMS	Min.	Max.
N/S ARC							
4	47	164.5	164.5	0.01	0.92	-2.28	1.35
6	70	164.9	164.8	-0.01	0.91	-2.17	1.50
8	93	234.5	234.5	-0.02	0.92	-2.46	1.52
10	101	256.1	256.1	-0.01	0.98	-2.32	1.77
12	97	244.8	244.8	-0.04	1.41	-2.68	3.10
14	91	229.5	229.4	0.00	2.32	-6.96	6.26
16	89	224.3	224.3	0.14	5.29	-13.30	14.75
S/N ARC							
4	47	133.6	133.6	-0.01	0.89	-2.28	1.36
6	70	169.0	169.0	0.00	0.93	-2.43	1.59
8	93	163.1	163.1	0.00	0.90	-2.54	1.56
10	101	180.6	180.6	-0.01	0.97	-2.61	1.98
12	97	170.6	170.5	0.00	1.17	-3.42	3.14
14	91	160.4	160.3	-0.03	1.99	-5.04	4.94
16	89	158.6	158.4	-0.03	3.99	-8.93	10.78

We note from Table 4.1 that to filter the noise of mean 0 and standard deviation $1\mu\text{m/s}$, spline knot spacing of 10 seconds appears to be suitable. The spline function with this spacing was accordingly used to approximate $\dot{\rho}$ in all arcs. For 101 data points in each arc, mean of $\Delta\dot{\rho}$ ranged from -0.01 to $0.00\mu\text{m/s}$ and RMS $\Delta\dot{\rho}$ ranged from 0.92 to $1.04\mu\text{m/s}$. The first derivative of the spline function gave the $\dot{\rho}$ values. The $\dot{\rho}$ and $\dot{\rho}_s$ values for one S/N arc over the nominal longitude of 187°E . are shown in Figures 4.1 and 4.2 respectively. The variation in the $\dot{\rho}$ and $\dot{\rho}_s$ values will be discussed in Section 5.

Rummel (1980, pp. 13, 43) has discussed the corresponding precision of $\dot{\rho}$ based on the precision of ρ by comparison of the degree at which the signal to noise ratio becomes one in the two cases. For the present study with satellite altitude of 150 km, the above reasoning gives:

$$(4.2) \quad \sigma_{\dot{\rho}} \equiv \sigma_{T_2} = 0.05 \text{ mgals for } \sigma_{\rho} = 1\mu\text{m/s at } h = 150 \text{ km}$$

Accordingly, 0.05 mgals will be used for σ_{T_2} in equation (2.9), where $\underline{D} = \sigma_{T_2}^2 \underline{I}$.

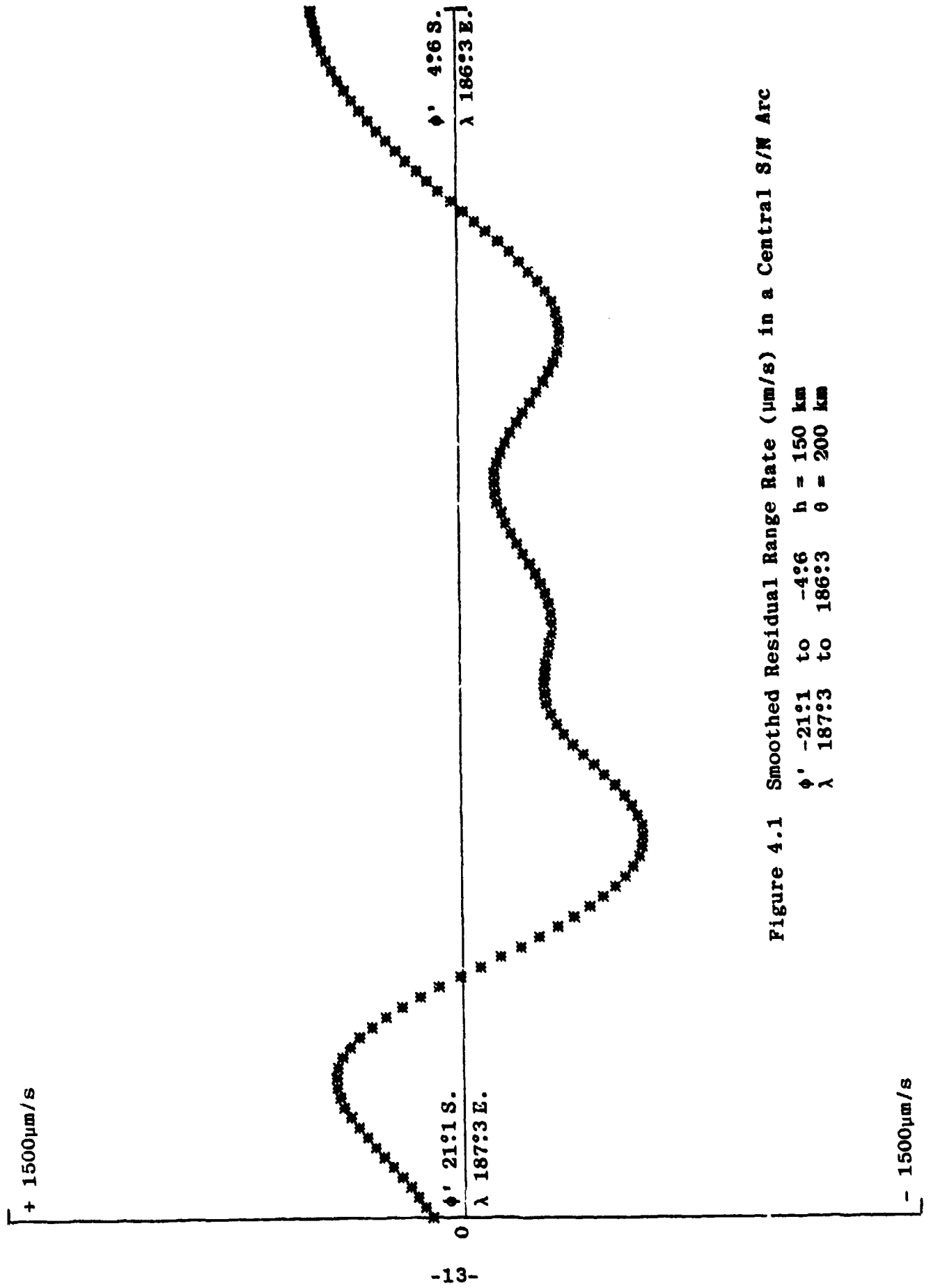


Figure 4.1 Smoothed Residual Range Rate ($\mu\text{m/s}$) in a Central S/N Arc

$\phi' -21^{\circ}1$ to $-4^{\circ}6$ $h = 150 \text{ km}$
 $\lambda 187^{\circ}3$ to $186^{\circ}3$ $\theta = 200 \text{ km}$

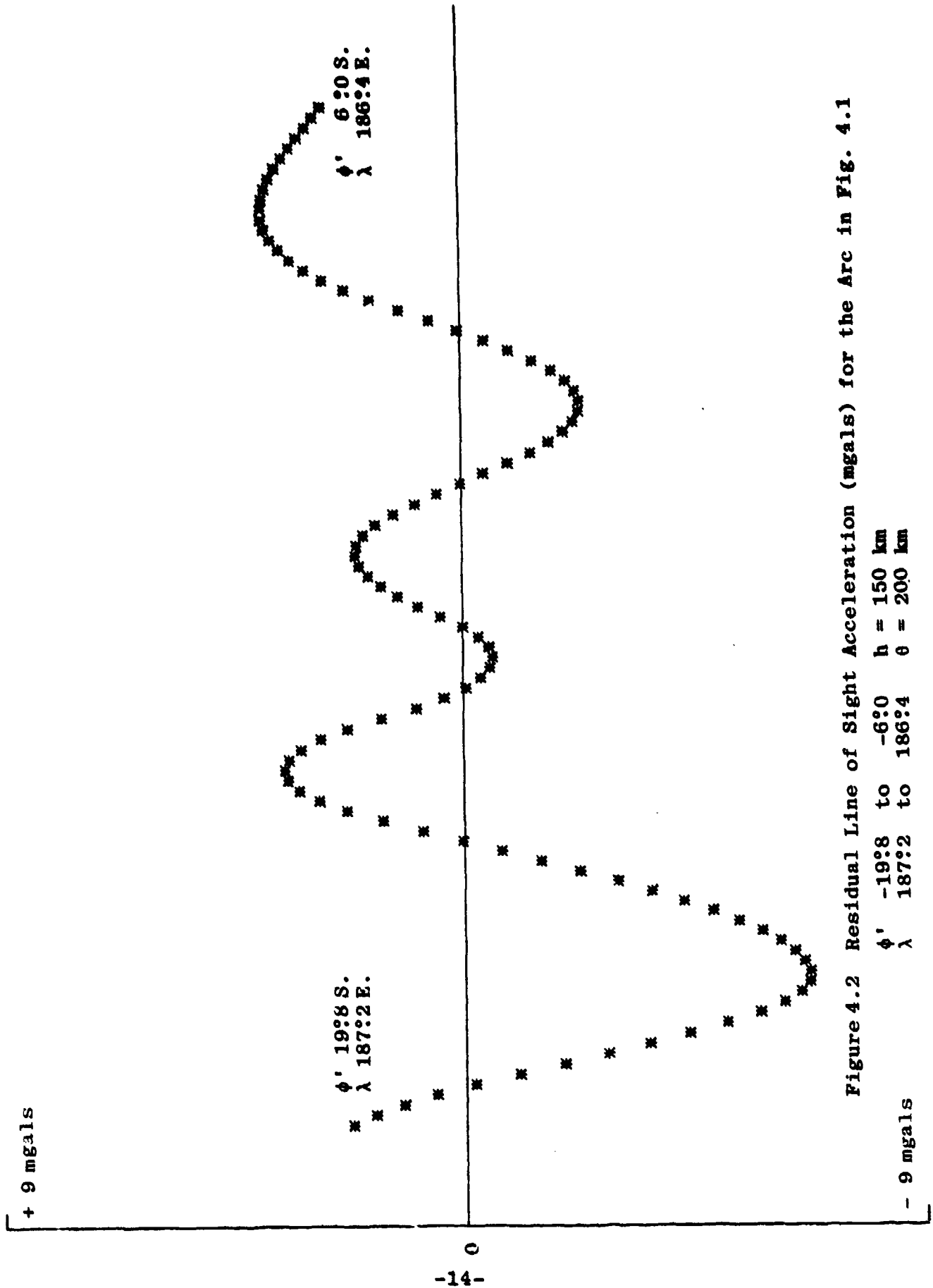


Figure 4.2 Residual Line of Sight Acceleration (mgals) for the Arc in Fig. 4.1

ϕ' -19:8 to -6:0 h = 150 km
 λ 187:2 to 186:4 θ = 200 km

5. Auto- and Cross-Covariance Functions

We need the covariances $\text{cov}(\underline{T}_l, \underline{T}_l)$ and $\text{cov}(\Delta g', \underline{T}_l)$ for predicting a residual anomaly $\Delta g'$ in equation (2.9):

$$(2.9) \quad \hat{\Delta g}' = \underline{C}_{\Delta g', \underline{T}_l}^T \underline{C}^{*-1} \underline{T}_l, \quad \underline{C}^* = \underline{C}_{\underline{T}_l, \underline{T}_l} + \underline{D}, \quad \underline{D} = \sigma_{\underline{T}_l}^2 \underline{I} \\ = \underline{A} \underline{T}_l$$

where \underline{A} is the estimating operator indicating the sensitivity of \underline{T}_l data in predicting the anomaly, or a weighting function (Breakwell, 1981), which may be examined to judge if distant data may be excluded without significantly affecting the predicted value.

We will accordingly examine the underlying covariances and the operator \underline{A} to see if a modest extent and density of data, which will be economical in computer time, will lead to a "satisfactory" prediction. The latter may be checked by the discrepancy, ϵ , of prediction $\hat{\Delta g}'$ compared to the input anomaly $\Delta g'$ used or implied in simulating the data:

$$(5.1) \quad \epsilon = \hat{\Delta g}' - \Delta g'$$

The computation of the covariances in (2.11) and (2.12) is somewhat simplified for the present study in view of Figure 3.3 and equation (3.4) for the direction cosines. We recall that for all data points i in N/S arcs, or the S/N arcs, the direction cosines at the two satellites 1,2 are:

$$(5.2) \quad \begin{aligned} a_{i1} &= a_{i2} = -0.015,318\dots = -a && \text{for both N/S and S/N arcs} \\ b_{i1} &= -b_{i2} = +0.999,882\dots = b && \text{for N/S arcs} \\ b_{i1} &= -b_{i2} = -0.999,882\dots = -b && \text{for S/N arcs} \\ c_{i1} &= c_{i2} = 0 && \text{for both N/S and S/N arcs} \end{aligned}$$

Accordingly the first vector transposed in (2.11) and (2.12) becomes: $[a, -by_{i2}, a, by_{i1}]$ for N/S arcs, and the sign of b is reversed for S/N arcs. Also, while modifying the units of covariances to be in mgals^2 for COVAX (see below (2.12)) if we multiply the covariances involving ξ and η by $-\gamma$, then using (2.7); equation (2.11) is changed to:

$$\begin{array}{c}
 \delta_{rj2} \quad \delta_{\phi'j2} \quad \delta_{rj1} \quad \delta_{\phi'j1} \\
 (5.3) \quad \text{cov}(T_{2i}, T_{2j}) \quad \cdot \quad \begin{bmatrix} (\delta_{r12}, \delta_{rj2}) & \cdot & \cdot & (\delta_{r12}, \delta_{\phi'j1}) \\ (\delta_{\phi'12}, \delta_{rj2}) & \cdot & \cdot & (\delta_{\phi'12}, \delta_{\phi'j1}) \\ (\delta_{r11}, \delta_{rj2}) & \cdot & \cdot & (\delta_{r11}, \delta_{\phi'j1}) \\ (\delta_{\phi'11}, \delta_{rj2}) & \cdot & \cdot & (\delta_{\phi'11}, \delta_{\phi'j1}) \end{bmatrix} \begin{bmatrix} a \\ b \\ a \\ -b \end{bmatrix} \\
 \equiv (T_{2i}, T_{2j}) \\
 = [a, b, a, -b] \cdot
 \end{array}$$

Similarly equation (2.12) is changed to:

$$\begin{array}{c}
 (5.4) \quad \text{cov}(T_{2i}, \Delta g') \quad \cdot \quad \begin{bmatrix} \delta_{r12}, \Delta g' \\ \delta_{\phi'12}, \Delta g' \\ \delta_{r11}, \Delta g' \\ \delta_{\phi'11}, \Delta g' \end{bmatrix} \\
 \equiv (T_{2i}, \Delta g') \\
 = [a, b, a, -b] \cdot
 \end{array}$$

In (5.3) and (5.4), the sign of b applies for N/S arcs; and it should be reversed for S/N arcs.

With two satellites each at points i and j, there are six distances (ψ) to be considered for the computation of covariances in (5.3). If $j=i$, the distance is either 0 or θ , the separation between the satellites. However, when $j \neq i$, the distances $i1-j1$, $i2-j2$, $i1-j2$, $i2-j1$ are, in general, all different.

For n data points, $n(n+1)/2$ covariances are required in the matrix \underline{C}_{T_2, T_2} and each element requires 16 calls to COVAX for the computation of (5.3). For the tests in this study, the covariances were rigorously computed to avoid any approximations in this regard. However, for production runs in future, interpolation from covariance elements stored in a table would be faster, e.g. see Sünkel(1979).

The $\text{cov}(T_{2i}, T_{2j})$ function has been plotted in Figure 5.1. This refers to residual line of sight accelerations at 150 km altitude, residual to degree 20, and a separation of 200 km between the satellites. The graph is comparable to the second curve in Figure 5a of Rummel (1980, p.19).

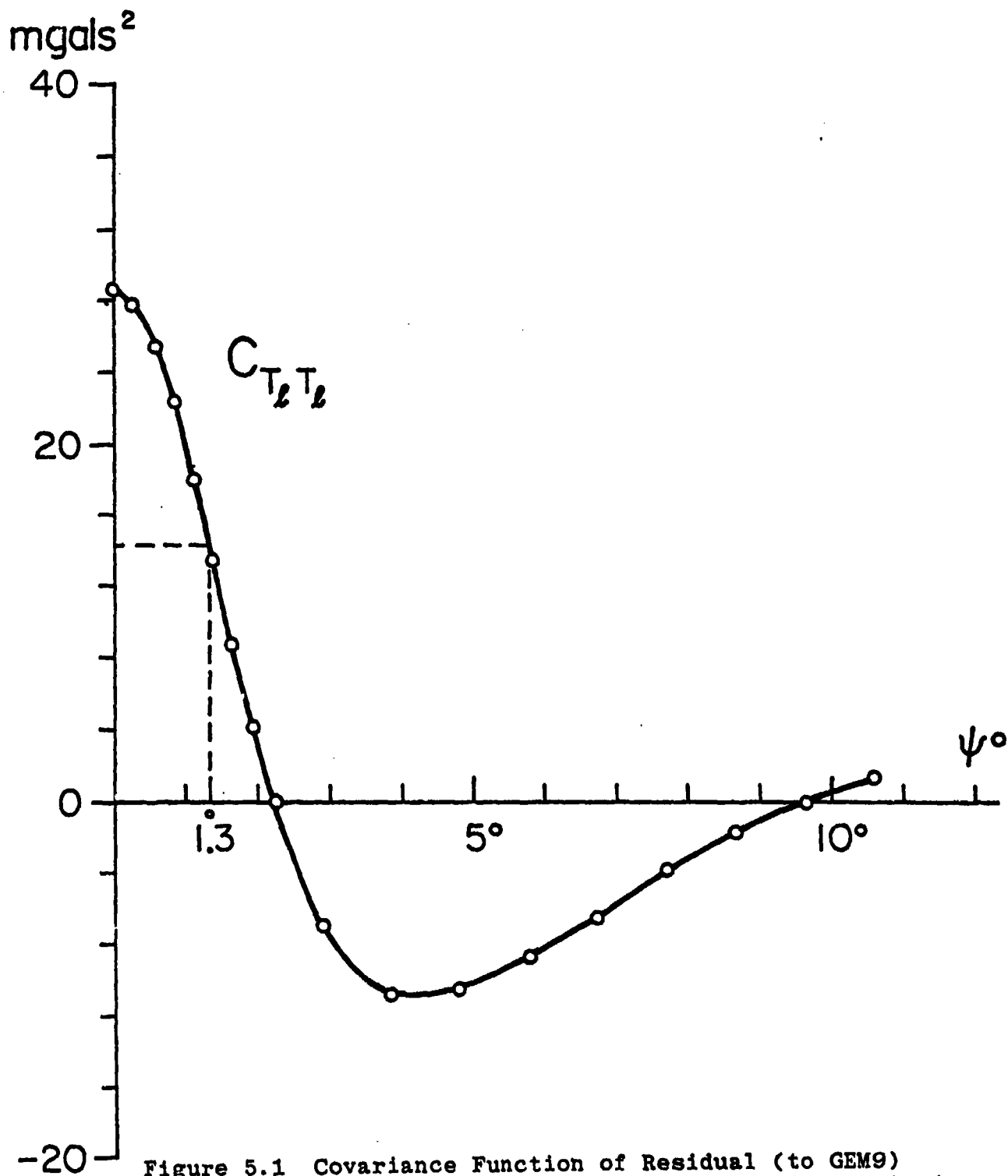


Figure 5.1 Covariance Function of Residual (to GEM9)
Line of Sight Acceleration. Satellite Altitude
150 km, Satellite Separation 200 km

The correlation length in our case is 1:3 so that the predicted anomaly would be most sensitive to T_{θ} data within $\psi = 1:3$ (Moritz, 1980, p.177). The extent of data will be numerically tested in Section 6.

The $\text{cov}(T_{\theta i}, \Delta g')$ function for one of the mean $1^{\circ} \times 1^{\circ}$ residual anomalies has been plotted in Figure 5.2. Similar graphs are obtained for other anomalies also. The two graphs in Figure 5.2 show the covariance of anomaly block $-13^{\circ} \geq \phi \geq -14^{\circ}$, $187^{\circ} < \lambda \leq 188^{\circ}$ with a N/S arc and a S/N arc each with nominal longitude $187:5$.

We note that the correlation length is 1:2; and that the peak of the covariance function does not occur when the lead satellite is over the center of the anomaly block, but when it is past the center by a distance of $\theta/2$, where θ is the separation between the satellites.

The location of the lead and trailing satellites and the anomaly block are specifically accounted for in (5.3) and (5.4), and the location of the measurement is specifically accounted for in (2.3) and (2.3). However, the graphs in Figure 5.2 imply that the selection of T_{θ} data (sensed at the lead satellite) should be centered (e.g. for a spherical distance $\psi = 1^{\circ} =$ correlation length) around a point which is down the arc at a distance $\theta/2$ from the anomaly block center. This agrees with Breakwell's interpretation (1981, p.10) of a data "point" as the mid-point between the two satellites at the time of a measurement.

We may also interpret this intuitively as shown in Figure 5.3. Unless the separation between the satellites is "small" compared to the anomaly block size, the lead satellite, or the trailing satellite, is primarily perturbed (Fig. 5.3a) when it is directly over the anomaly block. The relative range rate between the satellites varies at these two instances and hence a significant line of sight acceleration is sensed (Fig. 5.3b) at the lead satellite. Unless the separation between the two satellites is "large" compared to the anomaly block size, both satellites are perturbed between the two extreme locations in Figure 5.3a, and accordingly the data selection should be centered around a point midway between these locations as shown in Figure 5.3b. We have implicitly assumed here that there is an optimum separation distance compared to the anomaly block size of interest.

If we now wish to compare the data points in a N/S and S/N arc, both passing over the center of the anomaly block, to examine which data points are primarily affected by the anomaly block, then we may conceptually consider the "data point" to be midway between the two satellites. This is shown in Figure 5.3c.

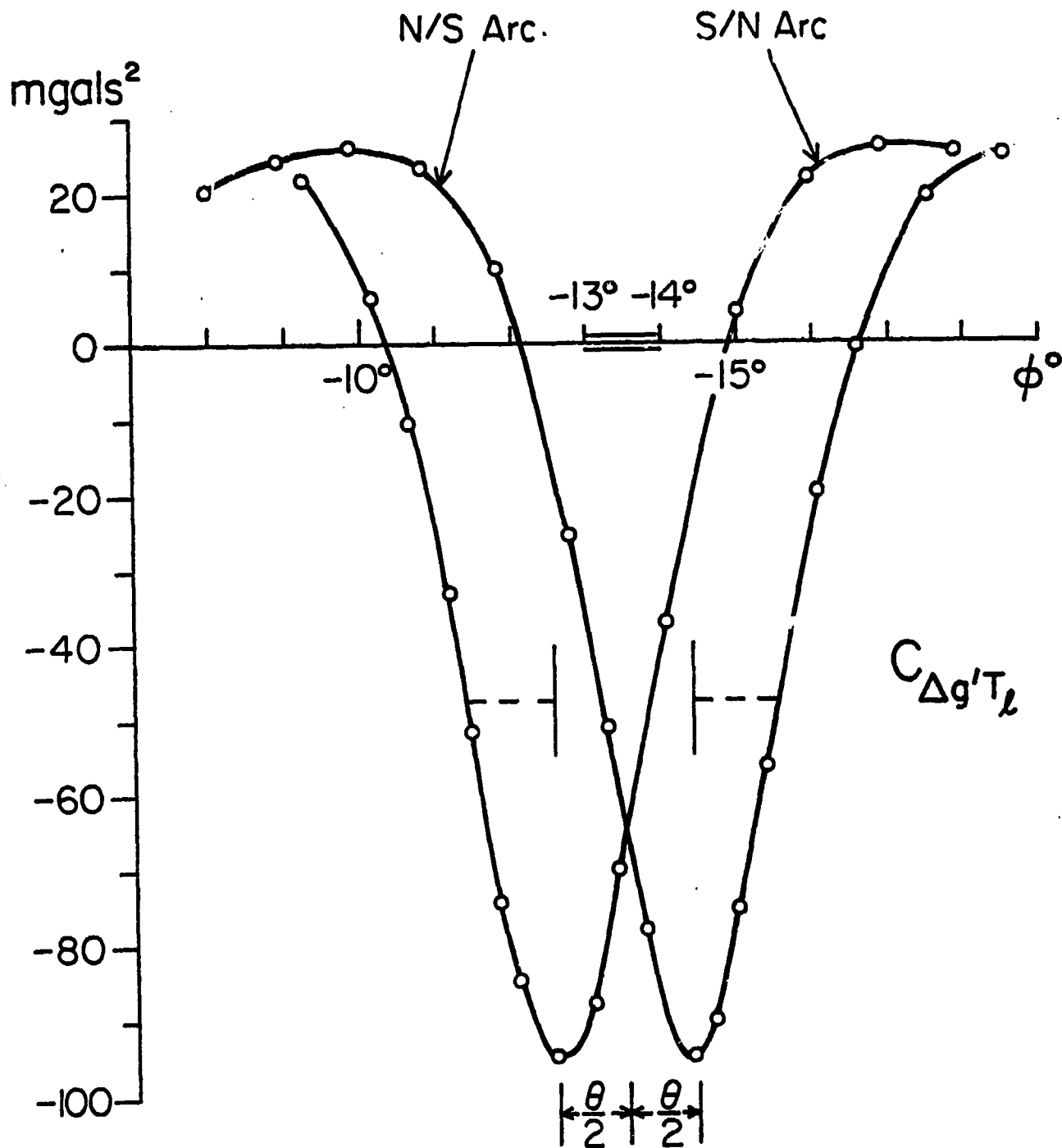


Figure 5.2 Cross-Covariance Function Between Surface Gravity Anomaly & Line of Sight Acceleration, Satellite Altitude 150 km, Satellite Separation 200 km ($=\theta$). Anomaly and Acceleration Residual to GEM9

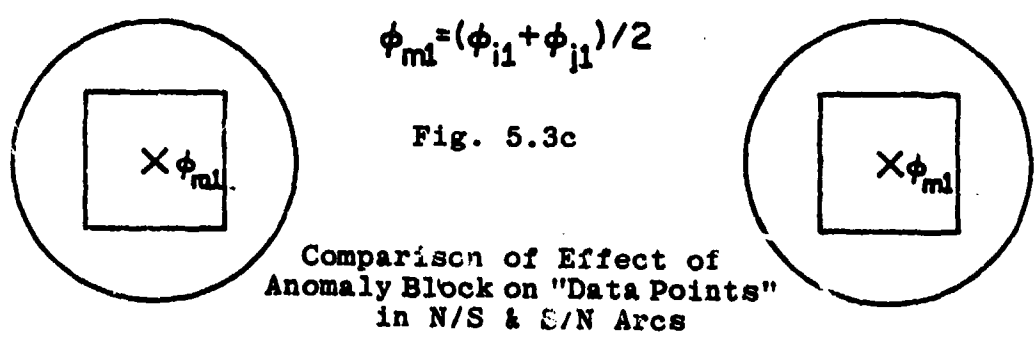
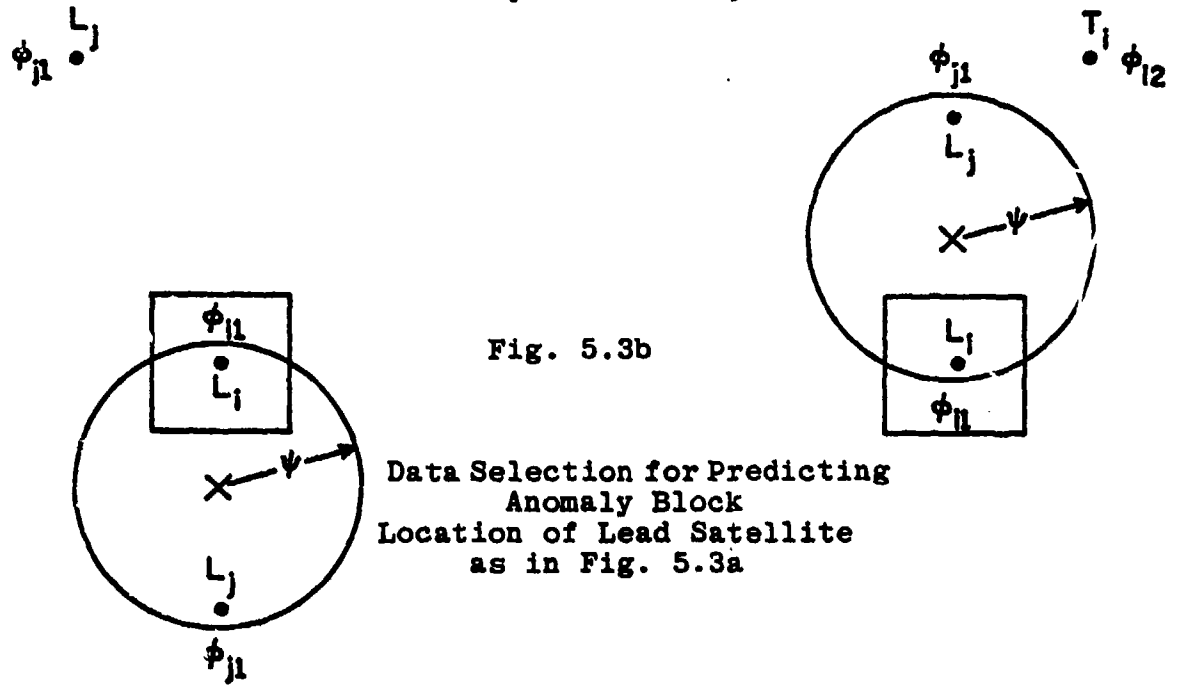
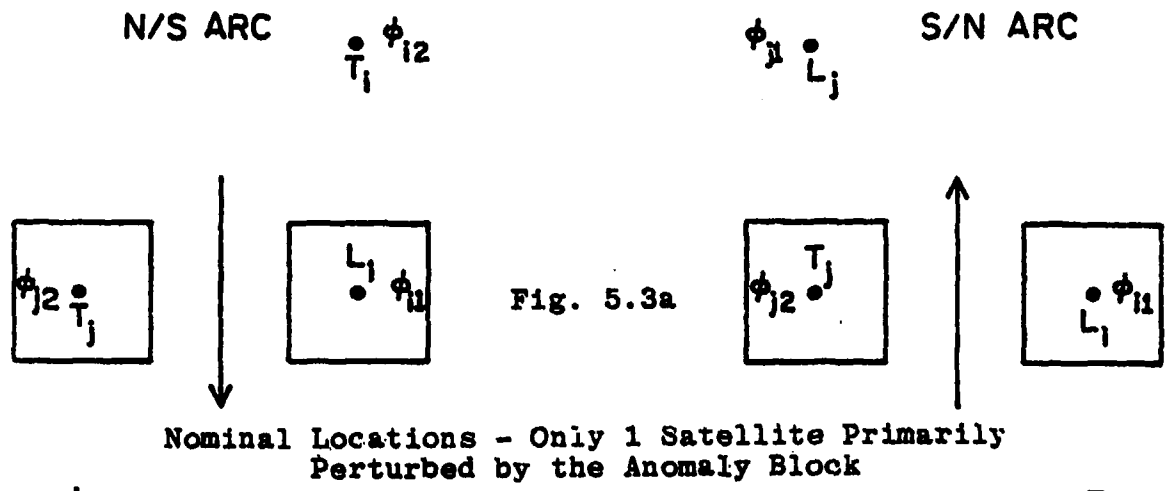


Figure 5.3 Data Selection for Predicting Anomaly Block & Comparison of "Data Points" for N/S & S/N Arcs

We should again point out that the location of data points remains at the location of lead satellite in accordance with (2.6) and (2.3) and the actual location of the two satellites is used to compute the covariances in (5.3) and (5.4). However, the selection of data points for predicting an anomaly block is done for a specified ψ , as shown in Figure 5.2. It is only for comparison of data points in N/S arcs, as compared to S/N arcs, to see the effect of anomaly blocks on these data points that we need to consider the "data point" as midway between the two satellites.

The comparison of $\dot{\rho}$ and $\ddot{\rho}$ data over N/S and S/N arcs is shown in Figures 5.4a,b and 5.5a,b respectively. First of all, we notice from Figure 5.5 that there is no discernible difference at few tenths of a mgal level between the accelerations caused by the anomaly blocks whether it is for N/S or S/N arcs. This is as it should be. The variation of acceleration due to the gradient of the anomaly field will be considered in Section 7.

However, we note from Figure 5.4 that though the broad pattern of range rate (which in fact reflects the variation of $\dot{\rho}$, i.e., $\ddot{\rho}$) is similar, there are very large difference of range rates in N/S and S/N arcs. It varies over the area from -1.5 to +1.9 mm/s. It is not clear if this variation is only due to the satellites in the N/S and S/N arcs traversing different gravity field before they reach a common location (for comparison), and we should expect this variation. Or is it also due to orbital errors introduced in the arcs. Wong and Sjogren (1980, p.14) describe that perturbations of the order of 0.5 m were added to some arcs in the radial direction which could cause perturbation in $\dot{\rho}$ of the order of -630 to -930 $\mu\text{m/s}$ over a span of 25° . As this span is traversed in 6 $\frac{1}{2}$ min. (≈ 390 s), a variation of 300 $\mu\text{m/s}$ in $\dot{\rho}$ will result in a variation of only 0.08 mgals in $\ddot{\rho}$. This only reflects the fact that orbital errors cause long wavelength perturbations in $\dot{\rho}$ and these are largely filtered out in computing $\ddot{\rho}$. (For some numerical results, see Hajela, 1977, p.64). It could not be confirmed if the data tape received by us had any orbital errors introduced or not.

We finally consider the estimating operator or weighting function $A = C^T \Delta_{g,T} C^{-1}$ in equation (2.9). Figure 5.6a,b show a plot of this function for a N/S and a S/N arc passing centrally over the $1^\circ \times 1^\circ$ anomaly block $-13^\circ \geq \phi \geq -14^\circ$, $187^\circ \leq \lambda \leq 188^\circ$ (cf Fig. 5.2). We notice again that the peak of the function is displaced down the arc from the center of anomaly block by one-half the separation between the satellites. Secondly, the prediction of anomaly block is most sensitive to data points within $\psi = 1^\circ$ from this peak. This interval has been marked on the zero lines of Figure 5.6a,b. Thirdly, the weighting function fluctuates with decreasing amplitude as we go farther from the center.

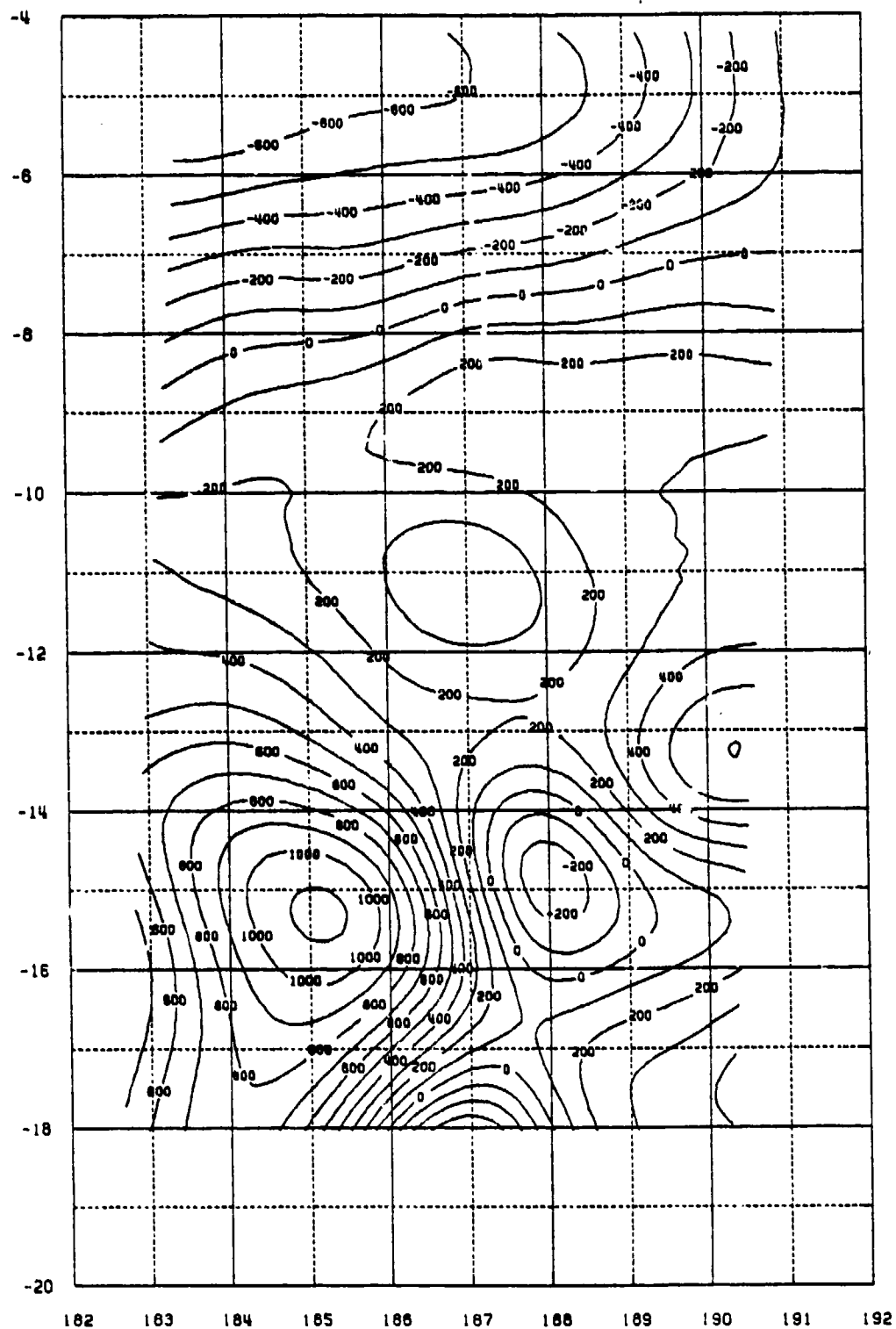


Figure 5.4a Residual (to GEM9) Range Rate Data in N/S Arcs
 Contour Interval 100 $\mu\text{m/s}$
 Satellite Altitude 150 km, Satellite Separation 200 km

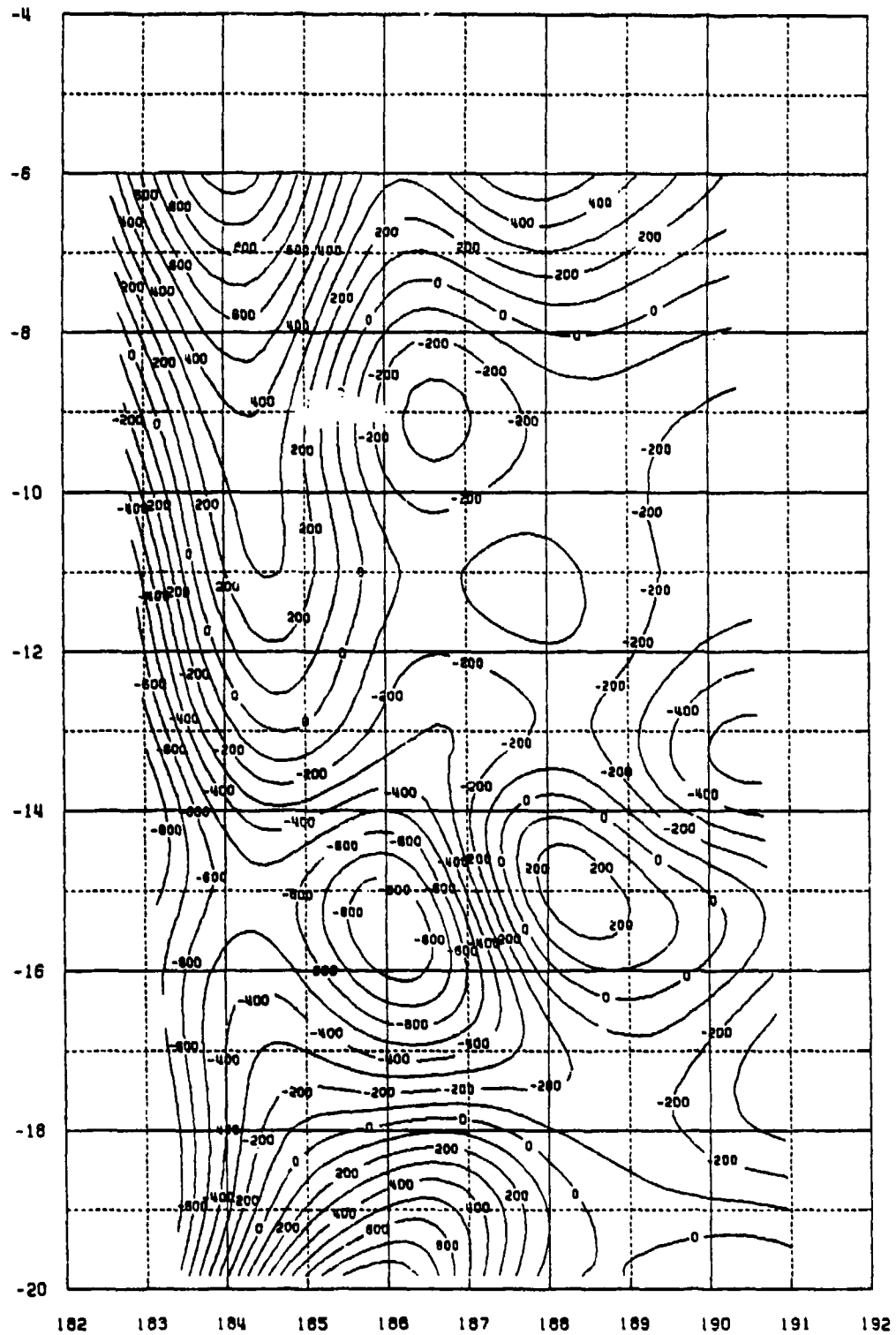


Figure 5.4b Same as Figure 5.4a for S/N Arcs

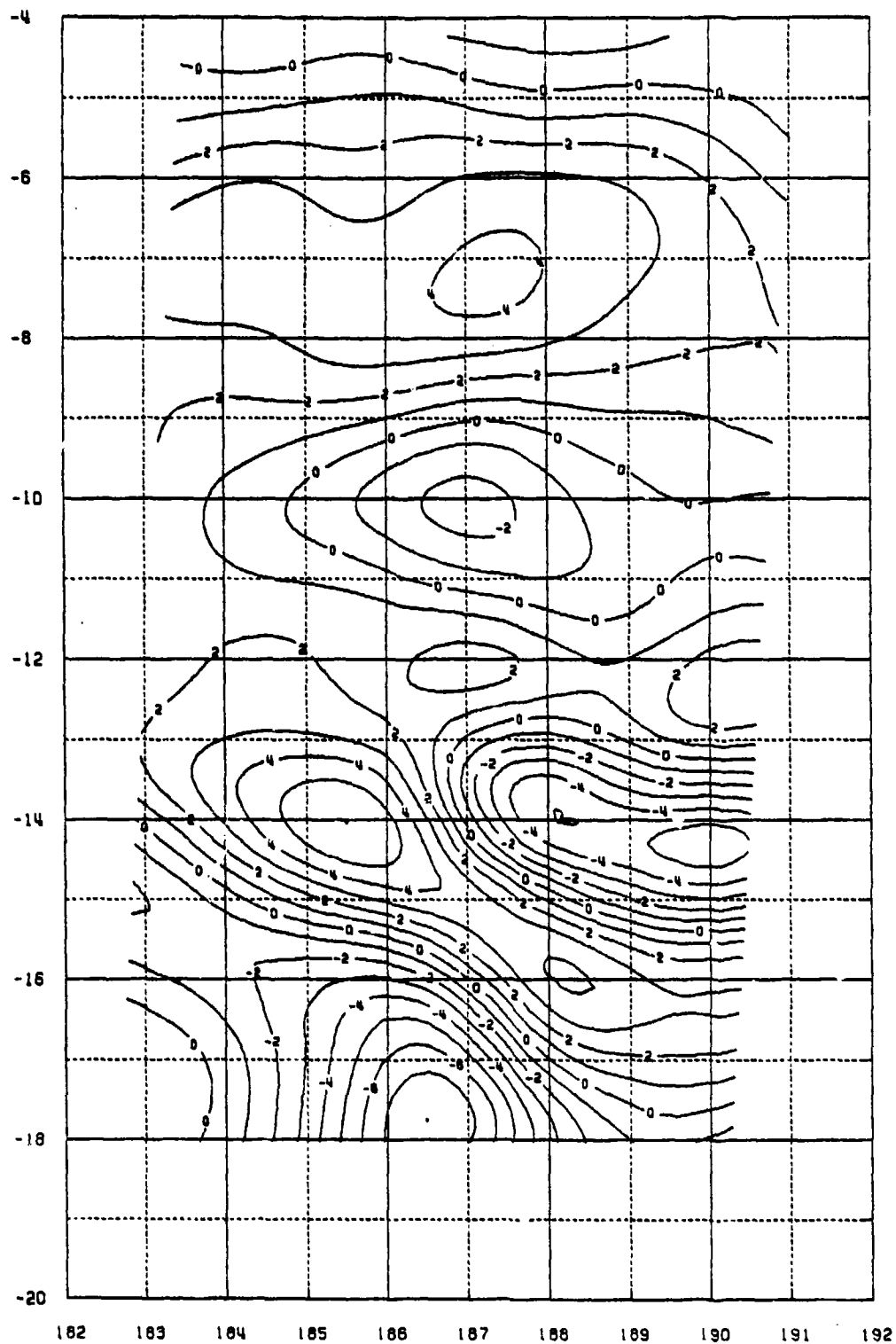


Figure 5.5a Residual Line of Sight Acceleration in N/S Arcs
 Contour Interval 1 mgal
 Satellite Altitude 150 km, Satellite Separation 200 km

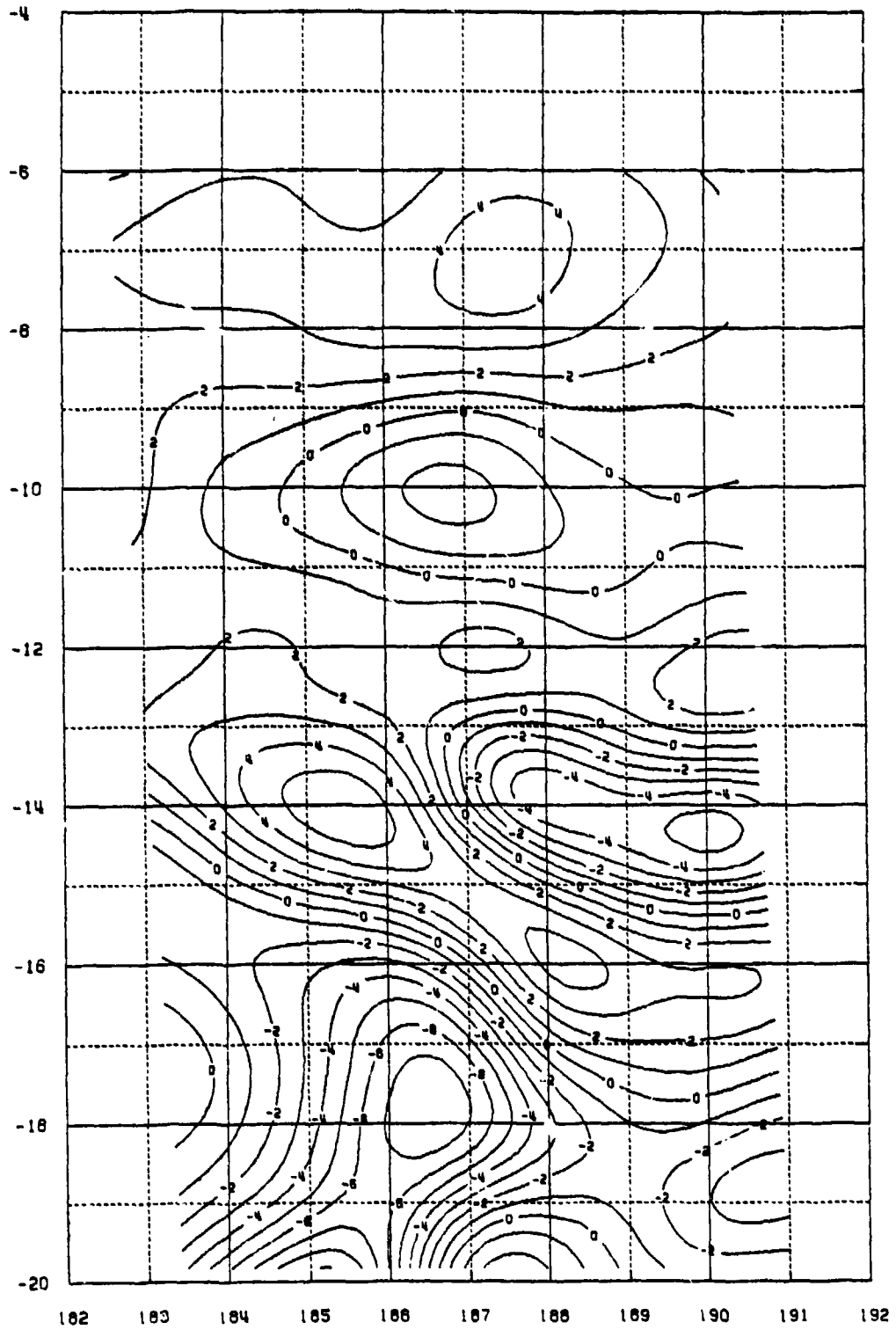


Figure 5.5b Same as Figure 5.5a for S/N Arcs

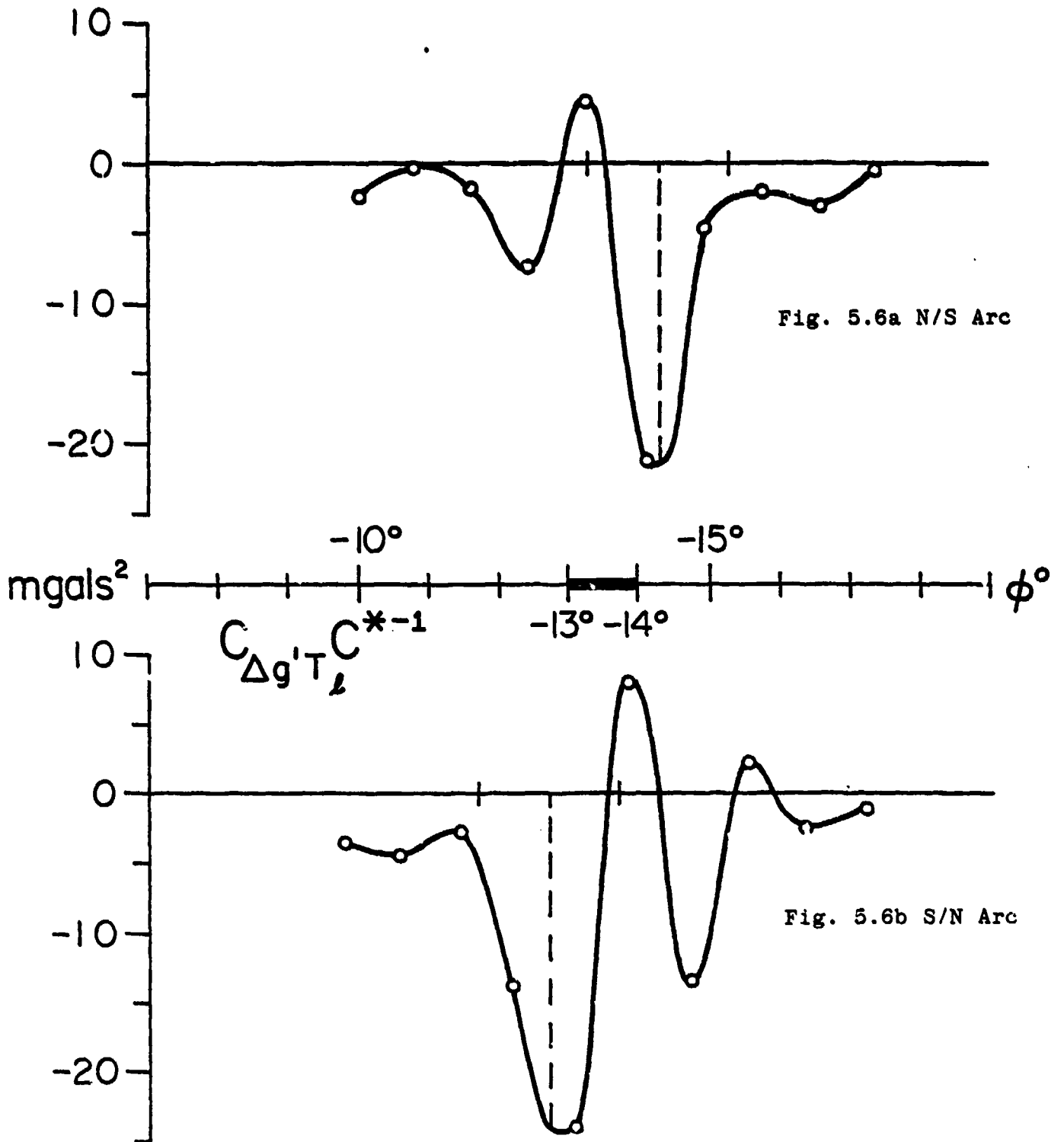


Figure 5.6 Estimating Operator or Weighting Function for $1^{\circ} \times 1^{\circ}$
 Mean Residual Anomalies from Residual (to GEM9)
 Line of Sight Accelerations ($\sigma_{T_{\Delta}} 0.05 \text{ mgals}$)
 Satellite Altitude 150 km, Satellite Separation 200 km

Note: The dashed line is at $\theta/2$ from center of anomaly block
 (see p.21 last para.)

This reflects not only the instability of the weighting function contributed by C^{*-1} , but also the fact that besides the contribution of farther points being smaller, it also tends to largely cancel out. It should therefore be adequate for "satisfactory" prediction, see equation (5.1), to restrict the extent of data to $\psi = 1^\circ$. This will lead to a modest requirement of data resulting in economy in computer time.

The instability, evidenced by large fluctuations of the weighting function was examined for different noise levels, i.e., σ_{T_2} (see equation 4.2). The weighting function had increasingly larger fluctuations as σ_{T_2} was decreased to 0.03, 0.02 and 0.01 mgals. This is obviously due to poor inversion of C^{*-1} as with the decrease of diagonal elements of D in (2.9), C^* does not remain diagonally dominant. On the other hand, with increase of σ_{T_2} to 0.10, 0.15, 0.20 mgals the weighting function gets increasingly damped. We have thus a numerical confirmation of (4.2), i.e. the standard deviation of T_2 being 0.05 mgals for the data used by us. We have to also ensure the symmetry of data and a balance between the density of data and the number of points used for the stability of the estimating operator, e.g. see Rummel et al. (1979, p.355). Finally, it is interesting to compare Figure 5.6 with the plot of theoretical weighting function in Breakwell (1981), which shows similar behavior.

6. Numerical Tests for Data Configuration

The 30'x30' mean residual anomalies in Figure 3.1 which were used to simulate δ (and thus the $\ddot{\delta}$) data may be meant to form 1°x1° (and 2°x2°) mean anomalies:

$$(6.1) \Delta g' = \Sigma(\Delta g_i \cos \phi_{mi}) / \Sigma(\cos \phi_{mi})$$

where the Δg_i on the right side is for 30'x30' anomalies with mean latitude ϕ_{mi} and $\Delta g'$ on the left hand side is for the mean anomaly of the larger 1°x1° (and 2°x2°) blocks.

The 1° mean residual anomalies are shown in Figure 6.1, and the gradient of the 1° anomaly field is shown in Figure 6.2 with a contour interval of 10 mgals. We again notice that the anomaly field is comparatively smooth from the north edge up to 12° S., becomes rough as we approach the trench which starts around 14° S. and proceeds south along the nominal longitude of 187°5 E.

We will now examine the prediction of two 1° residual anomalies #1, $-13^\circ \geq \phi \geq -14^\circ$, $187^\circ \leq \lambda \leq 188^\circ$, +51 mgals and #2, $-15^\circ \geq \phi \geq -16^\circ$, $187^\circ \leq \lambda \leq 188^\circ$, -99 mgals. The first is a large positive anomaly just outside the trench,

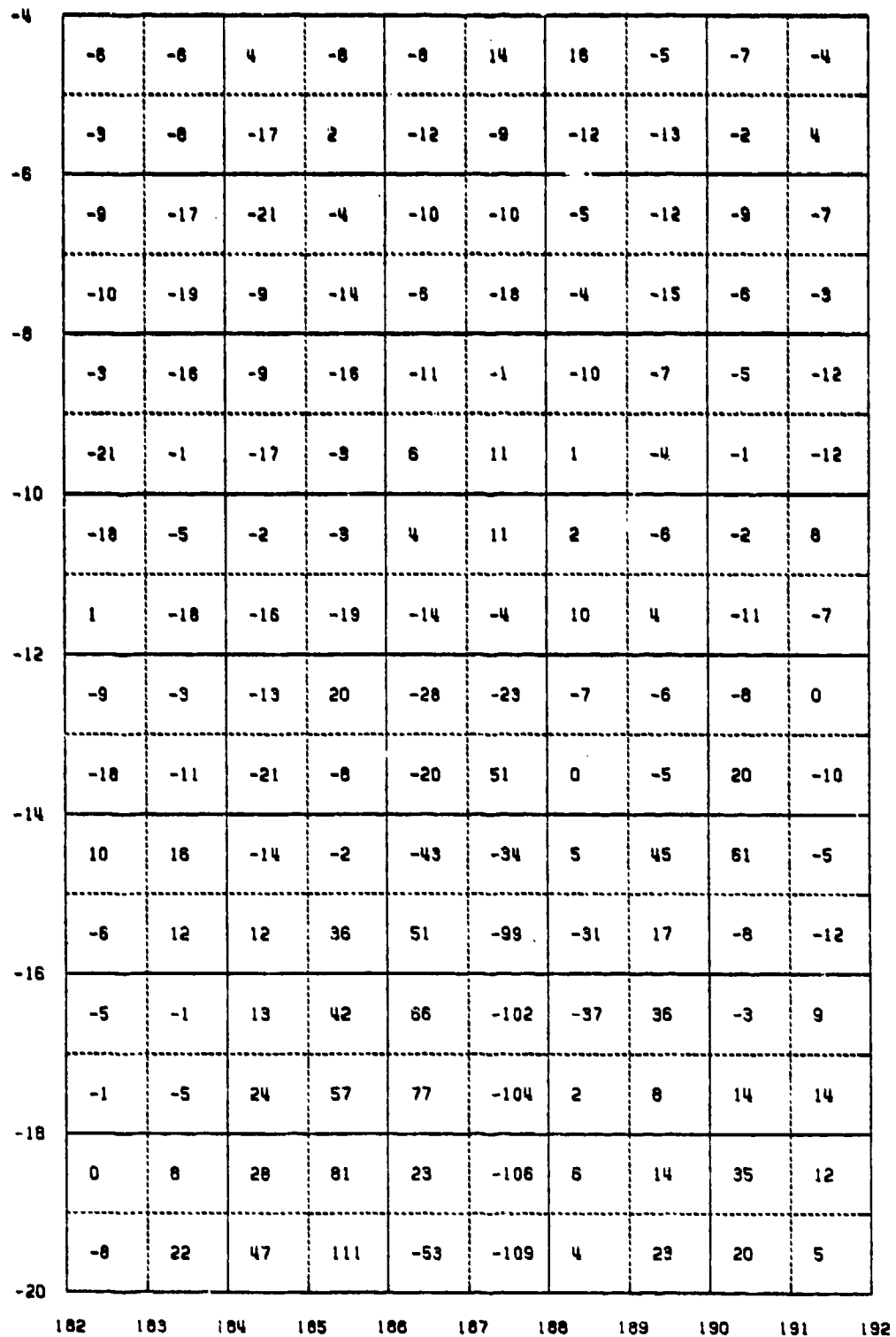


Figure 6.1 1°x1° Mean Residual (to GEM9) Anomalies in mgals.
 These anomalies are obtained from 30'x30' anomalies
 in Figure 3.1.

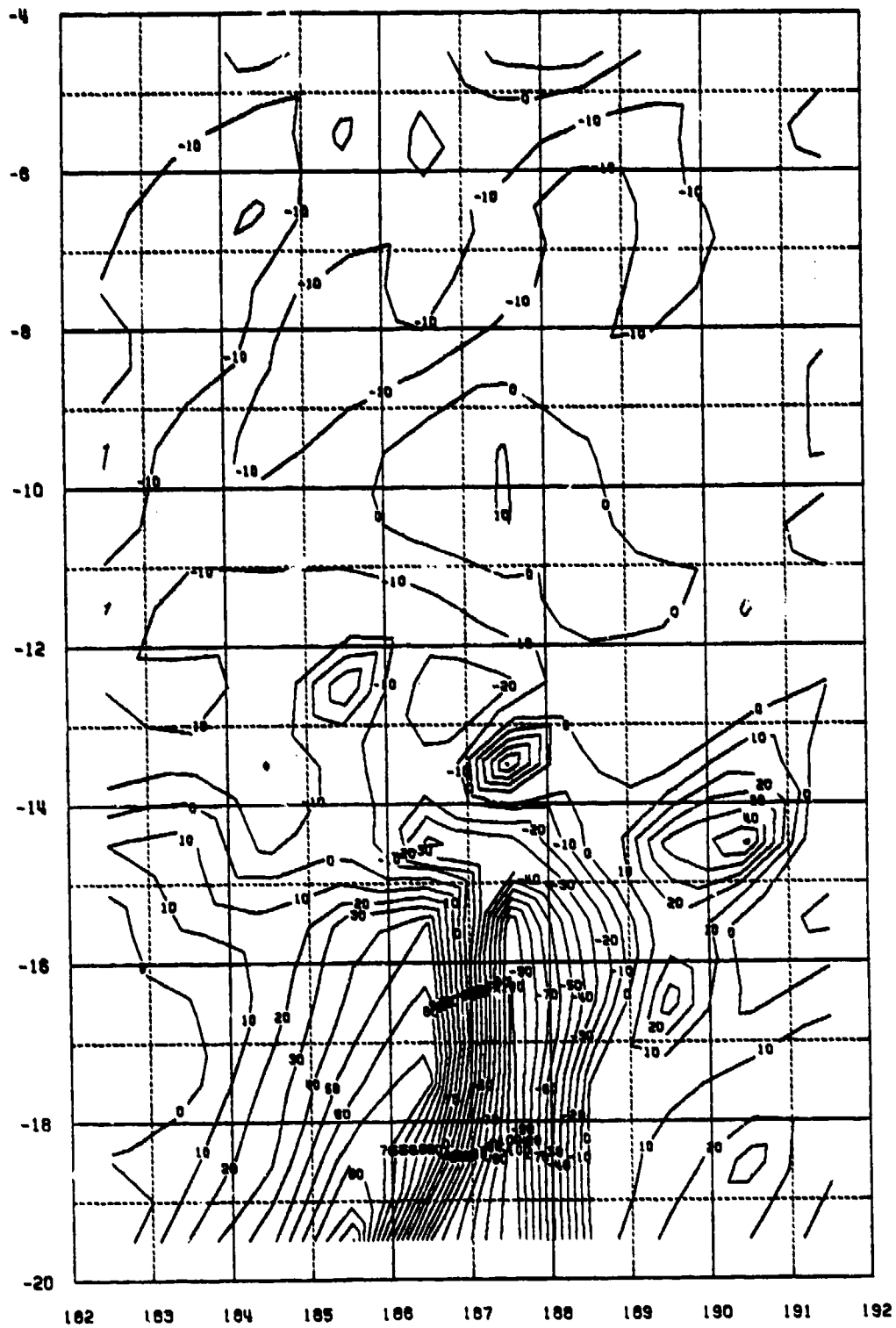


Figure 6.2 Gradient of the $1^{\circ} \times 1^{\circ}$ Mean Residual Anomalies.
Contour Interval 10 mgals.

while the second is a large negative anomaly just inside the trench. We will in particular test the effects of the extent and density of data on the prediction by examining (5.1) and try to determine a modest data requirement for economy in computer time consistent with satisfactory prediction. Both the N/S and the S/N arcs would be used to confirm the results, while taking into account the selection of data points as shown in Figure 5.3b.

Each anomaly was predicted separately with data arranged symmetrically for that anomaly. This has been done throughout in this study. Initially, some tests were made to examine the correlations between adjacent anomalies by predicting several anomalies together. The correlations were of the order of 0.2 to 0.6 as already reported in the error analysis by Rummel (1980, e.g. Table 4, p.31). Also, as the prediction of several anomalies together by a common data set did not result in optimally symmetric arrangement of data for the individual anomalies, further tests for correlations were not useful in this simulation study where we could individually examine the prediction discrepancy (5.1) for each anomaly.

Table 6.1 shows the effect of the extent of data on the prediction, where we have used \bar{p} data for $\psi = 0:5, 1^\circ, 1:5, 2:5, 3:5$. The predicted anomaly $\Delta g'$, prediction discrepancy ϵ , and the estimated standard deviation of prediction $\hat{\sigma}_{\Delta g'}$ are tabulated using (2.9), (5.1) and (2.10). The results are given only for $\sigma_{\bar{p}} = 0.05$ mgals, though other values were also tried.

Table 6.1 confirms the conclusions from Figure 5.6 that data beyond $\psi = 1^\circ$ does not alter the predicted value much; in fact for these two anomalies the prediction discrepancy ϵ is least at $\psi = 1^\circ$. Secondly, $\hat{\sigma}_{\Delta g'}$ is a nominal estimate of the standard deviation of prediction depending primarily on the number of data points and their geometry. $\hat{\sigma}_{\Delta g'}$ should thus be interpreted with caution, e.g. for the case of #2 anomaly. The prediction discrepancy, ϵ , when available, is a better criterion for judging the accuracy of prediction. Thirdly, we note that the predicted value of #2 anomaly is very discordant. The reason for this will become clear later in Section 7. However, Table 6.1 does show that in this case also, the extent of data beyond $\psi = 1^\circ$ does not alter the predicted value much. This was borne out by other tests also with $\psi = 4^\circ, 5^\circ, 6^\circ$.

Table 6.2 shows the effect of the density of data points on the prediction. The results are given for $\sigma_{\bar{p}} = 0.05$ mgals. Apparently, there is no variation in the prediction discrepancy if the data grid is more dense than about $0:4 \times 0:4$. This agrees with the ideas of Sünkel (1981, p.91) that there is no improvement in prediction error estimation if the data grid density is increased beyond one-third

Table 6.1 Variation in the Predicted Mean 1°x1° Residual Anomaly with Variation in Extent (ψ°) of $\bar{\rho}$ Data

$\sigma_{\bar{\rho}} = 0.05 \text{ mgals}, \quad \sigma_{\bar{\rho}} = 1 \mu\text{m/s}$

ψ°	Arcs	No. & Spacing of $\bar{\rho}$ Data			Predicted Residual Anom. (mgals)		
		#	$\Delta\lambda^\circ$	$\Delta\phi^\circ$	$\hat{\Delta g}'$	ϵ	$\hat{\sigma}_{\Delta g}'$
#1 Anom. $\Delta g' = +51 \text{ mgals}$							
0:5	N/S	14	0.20	0.28	51	0.4	13.0
1:0	"	21	0.40	0.41	49	-2	12.3
1:5	"	21	0.60	0.55	55	5	12.0
2:5	"	36	0.80	0.69	64	14	10.9
3:5	"	48	1.00	0.83	62	11	11.0
0:5	S/N	15	0.20	0.28	44	-7	13.0
1:0	"	19	0.40	0.41	55	4	12.4
1:5	"	23	0.60	0.55	58	7	11.6
2:5	"	34	0.80	0.69	58	8	11.0
3:5	"	48	1.00	0.83	60	10	10.5
#2 Anom. $\Delta g' = -99 \text{ mgals}$							
0:5	N/S	16	0.20	0.28	-36	63	12.9
1:0	"	18	0.40	0.41	-34	64	12.8
1:5	"	21	0.60	0.55	-29	70	12.0
2:5	"	37	0.80	0.69	-29	69	10.7
3:5	"	44	1.00	0.83	-26	72	11.1
0:5	S/N	14	0.20	0.28	-36	63	13.0
1:0	"	21	0.40	0.41	-38	61	12.4
1:5	"	22	0.60	0.55	-35	63	11.6
2:5	"	38	0.80	0.69	-35	64	10.8
3:5	"	49	1.00	0.83	-41	58	10.3

Table 6.2 Variation in the Predicted Mean 1°x1° Residual Anomaly with Variation in Density of $\bar{\rho}$ Data

$\sigma_{\bar{\rho}} = 0.05 \text{ mgals}, \quad \sigma_{\bar{\rho}} = 1 \mu\text{m/s}$

ψ°	Arcs	No. & Spacing of $\bar{\rho}$ Data			Predicted Residual Anom. (mgals)		
		#	$\Delta\lambda^\circ$	$\Delta\phi^\circ$	$\hat{\Delta g}'$	ϵ	$\hat{\sigma}_{\Delta g}'$
#2 Anom. $\Delta g' = -99 \text{ mgals}$							
1:0	N/S	18	0.40	0.41	-34	64	12.8
"	"	29	"	0.28	-33	66	12.4
"	S/N	21	"	0.41	-38	61	12.4
"	"	30	"	0.28	-38	61	12.3
0:5	N/S	16	0.20	0.28	-36	63	12.9
"	"	31	"	0.14	-37	62	12.8
"	S/N	14	"	0.28	-36	63	13.0
"	"	29	"	0.14	-37	62	12.8

of the correlation length of the underlying covariance function, which for our case is about $1:2$ to $1:3$ (Fig. 5.2 and 5.1 respectively). Our results are also in general agreement with Rummel et al. (1979, Fig. 2, p. 357), who found the optimum spacing of data grid at 250 km altitude to be $0:5 \times 0:5$ for predicting 1° anomalies.

An additional test was tried to combine the extent and density of data by having a $0.2^\circ \times 0.3^\circ$ grid ($\Delta\lambda \times \Delta\phi$) till $\psi = 0:5$, a $0:4 \times 0:4$ grid for $0:5 < \psi < 1:0$, a $0:8 \times 0:7$ grid for $1:0 < \psi < 2:5$, but it did not lead to any improvement over a grid of $0:4 \times 0:4$ for $\psi = 1^\circ$.

We thus have a very modest data requirement leading to economical data processing. With $\ddot{\rho}$ data and location of satellites on tape, several anomalies could be predicted one at a time in the same run with data being selected optimally for each anomaly as in Figure 5.3b. The average run time on Amdahl 470 V/6-II computer was 12 seconds for predicting each $1^\circ \times 1^\circ$ mean anomaly. This time due to the rigorous computation of the covariances could be considerably reduced by interpolation from stored tables, as discussed in the beginning of Section 5.

7. Prediction of $1^\circ \times 1^\circ$ Mean Residual Anomalies

The optimum data configuration from Sections 5 and 6 for predicting 1° mean anomalies is then to use $\ddot{\rho}$ data in a symmetric grid of $0:4 \times 0:4$ for $\psi = 1^\circ$ around a point which is down the arc from the center of anomaly block by a distance equal to one-half the separation between the satellites.

An explanation for the large prediction discrepancy for #2 anomaly in the trench (see Fig. 6.2) may be the very sharp gradient of the anomaly field. If we compare the anomaly field in Figure 6.1 with the accelerations in Figure 5.5, it is apparent that the satellite is sensing the "highs" in the anomaly field of 51 mgals at $13:5$ S., $187:5$ E. (#1 anomaly) and that of 77 mgals at $17:5$ S., $186:5$ E. The intervening feature of #2 anomaly at $15:5$ S., $187:5$ E. is being sensed in Figure 5.5, but is considerably smoothed out because of the two "highs" on either side.

To confirm this presumption, we may examine several anomalies in the comparatively smooth field away but near the trench and then extend this sample to the rough anomaly field as we approach the trench and also consider anomaly blocks over the trench. Table 7.1 shows 24 predicted anomalies in the area bounded by latitudes 8° to 12° S. and longitudes 184° to 190° E. The $\ddot{\rho}$ data density is

0°4x0°4 with extent $\psi = 1^\circ$, and the results are for σ_g as 0.05 mgals. The data is selected symmetrically individually for each anomaly as shown in Figure 5.3b.

The anomalies are listed in N/S tiers by longitude to follow the pattern of $\ddot{\rho}$ data sensed by polar satellites. The RMS (root mean square) value of anomalies $\Delta g'$, predicted value $\hat{\Delta g}'$, and the prediction discrepancy ϵ is also listed in sets of eight anomalies. The minimum, maximum and mean value of ϵ is also listed for sets of eight anomalies. We also list the correlation coefficient r between the "true" value $\Delta g'$ and the predicted value $\hat{\Delta g}'$ of the 1° mean anomalies:

$$(7.1) \quad r = \frac{\sum_{i=1}^n (\Delta g' \cdot \hat{\Delta g}') / n}{\left(\sum_{i=1}^n \Delta g'^2 / n \right)^{\frac{1}{2}} \left(\sum_{i=1}^n \hat{\Delta g}'^2 / n \right)^{\frac{1}{2}}}$$

where n is the number of anomalies being compared.

We thus find very good agreement in this area between the input (1° anomalies obtained from input $30'$ anomalies) and the predicted 1° anomalies. For all 24 anomalies, the RMS value for the input $\Delta g'$, predicted $\hat{\Delta g}'$, and the prediction discrepancy ϵ are 9.5, 6.2 and 5.5 mgals respectively with a correlation coefficient r of 0.84. The nominal estimate of the standard deviation of 12.5 mgals is therefore pessimistic by a factor of about 2.3. This appears to be due to the use of a global covariance function in equation (2.13) instead of a local covariance function, because the former represents only the average accuracy of the estimated quantities. It is well known that the predicted quantity is not very sensitive to changes in the covariance function, but the estimate of standard deviation is strongly dependent on the covariance function. Schwarz and Lachapelle (1980, p.33) found that the standard errors from the global covariance function of Tscherning-Rapp (equation (2.13)) were about three times larger than they should be for Canada. Schwarz (1976, p.13) points out that for local applications, it is necessary that the local covariance function should fit the degree variances of the local anomaly gradients. This was not the case for the covariance function used in this study.

We now extend the prediction to the rough anomaly field as we approach and then enter the trench area. From Figures 6.2 and 6.1, we chose eight anomalies bounded by the latitudes 12° to 16° S. and longitudes 186° to 188° E. where the eastern anomalies are along the axis and then directly over the trench, and the western anomalies are immediately by the side of the trench. The particulars of prediction are listed in Table 7.2.

Table 7.1 Prediction of 1°x1° Mean Residual Anomalies in the Area 8°- 12° S., 184°- 190° E.
 Extent of $\bar{\rho}$ Data $\psi = 1^\circ$;
 Density of Data 0°4 x 0°4 ;
 $\sigma_{\bar{\rho}} = 0.05 \text{ mgals}$, $\sigma_{\bar{\rho}} = 1 \mu\text{m/s}$

seq. #	Center of Anom Block		Prediction of Anom. (mgals)				Statistics for ϵ (mgals)	Correln. Coeff. r
	ϕ_c°	λ_c°	$\Delta g'$	$\hat{\Delta g}'$	ϵ	$\hat{\sigma}_{\Delta g}'$		
1	-8.5	184.5	-9	-4	5	12.4	Min. -2 Max. 14 Mean 5.1	0.92
2	-9.5	"	-17	-7	10	"		
3	-10.5	"	-2	-2	0	"		
4	-11.5	"	-16	-7	9	12.7		
5	-8.5	185.5	-16	-10	6	12.4		
6	-9.5	"	-3	-5	-2	"		
7	-10.5	"	-3	-3	-1	"		
8	-11.5	"	-19	-5	14	12.8		
		RMS	12.5	6.0	7.4			
		Mean	-10.6	-5.5	5.1	12.5		
9	-8.5	186.5	-11	-4	7	12.4	Min. -2 Max. 11 Mean 2.5	0.82
10	-9.5	"	6	7	1	"		
11	-10.5	"	4	8	5	"		
12	-11.5	"	-14	-3	11	12.7		
13	-8.5	187.5	-1	-2	-2	12.4		
14	-9.5	"	11	11	0	"		
15	-10.5	"	11	11	0	"		
16	-11.5	"	-4	-6	-2	12.8		
		RMS	8.6	7.3	4.9			
		Mean	0.2	2.7	2.5	12.5		
17	-8.5	188.5	-10	-6	4	12.4	Min. -5 Max. 5 Mean 0.4	0.84
18	-9.5	"	1	-5	-5	"		
19	-10.5	"	2	2	0	"		
20	-11.5	"	10	11	1	12.7		
21	-8.5	189.5	-7	-2	5	12.4		
22	-9.5	"	-4	-3	2	"		
23	-10.5	"	-6	-5	1	"		
24	-11.5	"	4	0	-4	12.8		
		RMS	6.2	5.0	3.4			
		Mean	-1.3	-0.9	0.4	12.5		
		For all 24 anom. RMS Mean	9.5	6.2	5.5	12.5		0.84

Table 7.2 Prediction of 1°x1° Mean Residual Anomalies in the Area 12°-16° S. , 186° to 188° E.

Extent of $\bar{\rho}$ Data $\psi = 1^\circ$;
Density of Data 0.4 x 0.4 ;

$\sigma_{\bar{\rho}} = 0.05 \text{ mgals}$, $\sigma_{\bar{\rho}} = 1 \mu\text{m/s}$

seq #	Center of Anom. Block		Prediction of Anomaly (mgals)				Statistics for ϵ (mgals)	Correln. Coeff. r
	ϕ_c°	λ_c°	$\Delta g'$	$\hat{\Delta} g'$	ϵ	$\hat{\sigma}_{\Delta g'}$		
1	-12.5	186.5	-28	-9	19	12.5		
2	-13.5	"	-20	-20	-1	"	Min. -38	
3	-14.5	"	-43	-32	11	"	Max. 19	
4	-15.5	"	51	13	-38	"	Mean -2.2	0.87
		RMS	37.3	20.4	21.9			
		Mean	-9.9	-12.1	-2.2	12.5		
5	-12.5	187.5	-23	6	28	12.5		
6	-13.5	"	51	57	6	12.4	Min. 6	
7	-14.5	"	-34	18	52	12.5	Max. 71	
8	-15.5	"	-99	-28	71	"	Mean 39.3	0.63
		RMS	59.2	33.0	46.3			
		Mean	-26.2	13.1	39.3	12.5		

The reasons for the large prediction discrepancies are clear from Figure 7.1, where the "true" anomalies (implied by 30' anomalies used for simulating $\bar{\rho}$ data) are joined by full lines and the predicted anomalies are joined by dashed lines. The anomalies are shown in longitudinal profiles from 184°5 to 189°5 E. and cover the area from 8°S. to 16° S.; i.e. all anomalies listed in Tables 7.1 and 7.2. Two additional anomalies have been shown on each side of the profiles along the longitudes 186°5 and 187°5 E. We recall that the profile along 187°5 E. goes directly over the trench south of latitude 14° S., while the profile along 186°5 E. is just by the side of the trench.

We see from the above two profiles that the satellite clearly senses the "highs" and "lows" of the anomaly field, but the intervening features are smoothed. Notice particularly the anomalies along longitude 186°5 E. with centers at latitudes 10°5 S., 14°5 S. and 16°5 S. which have small prediction discrepancy but the intervening anomalies at 12°5 S. and 15°5 S. have large prediction discrepancy because the satellite does not sense the rapid variation in the anomaly gradient. Note that it is not the magnitude of the anomaly or the large anomaly gradient which causes prediction discrepancy (e.g. the anomalies with centers 14°5 S. and 16°5 S. and 17°5 S.) but the rapid variation in the anomaly gradient.

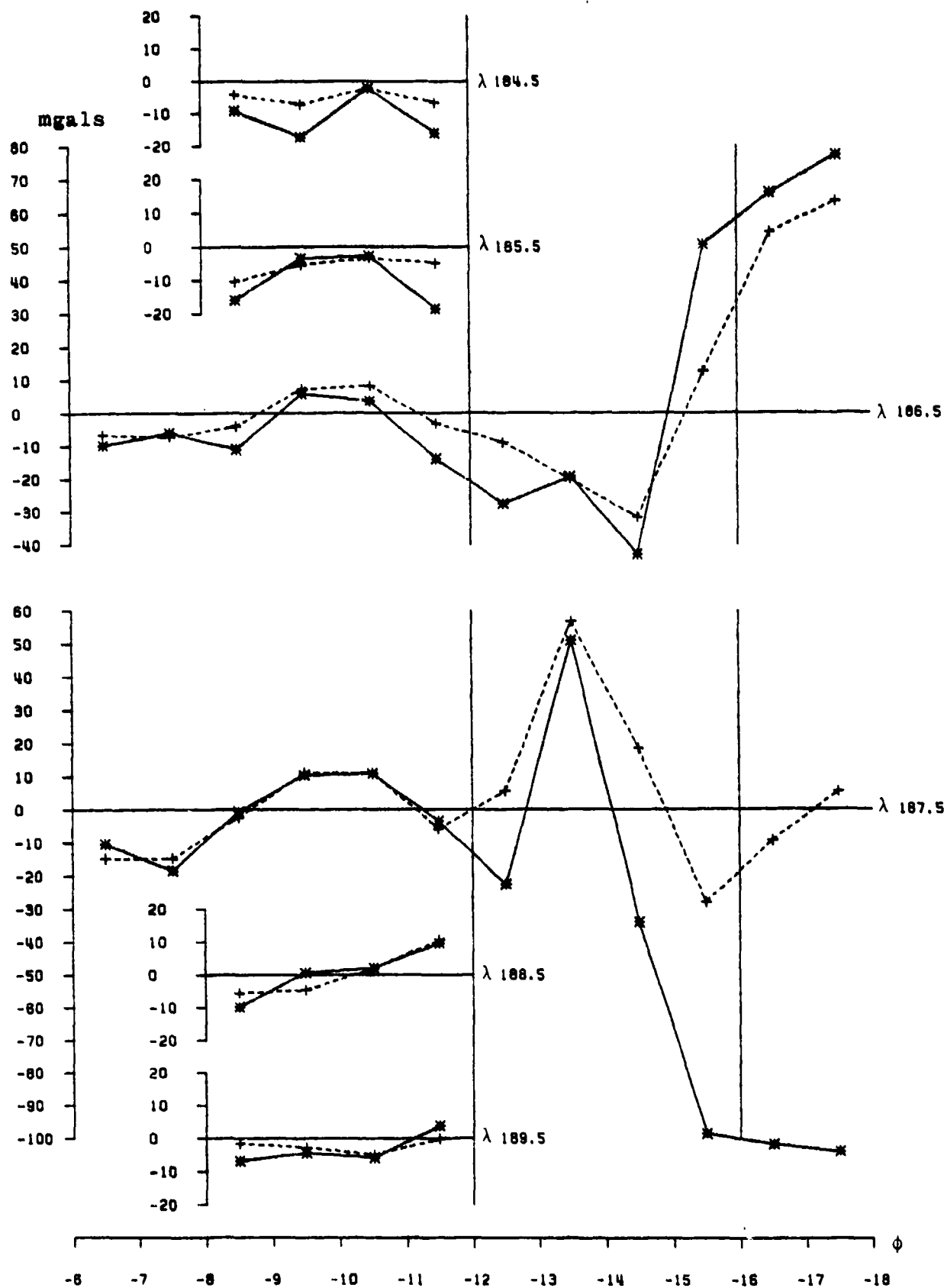


Figure 7.1 Prediction of $1^\circ \times 1^\circ$ Mean Residual Anomalies (mgals). $\sigma_{\rho} = 0.05 \text{ mgals}$, $\sigma_{\beta} = 1 \mu\text{m/s}$. "True" Anomalies (implied by $30'$ anomalies used for simulating β^{ρ} data) joined by full lines. Predicted anomalies joined by dashed lines. Extent of data $\psi = 1^\circ$; Density of data 0.4×0.4

This is again seen in the profile along longitude 187°5 E., where the anomalies with centers at latitudes 11°5 and 13°5 S. have small prediction discrepancy but the anomaly at 12°5 S. has a large discrepancy due to a negative anomaly gradient changing to a positive anomaly gradient at 12°5 S. The variation in the anomaly gradient is so rapid in the trench area after 15° S. that the predicted anomaly is nearly zero at 16°5 and 17°5 S. The rapid variation in the 1° anomaly gradient is seen in Figure 6.2. It is also instructive to see the variation of $\ddot{\rho}$ sensed at the satellite in this area in Figure 5.5b.

To confirm the presumption that it is the variation in the anomaly gradient that causes prediction discrepancy, and that it is not caused by lack of resolution at 1°x1° block size, we will examine the prediction of 30'x30' and 2°x2° anomalies in Sections 8 and 9 respectively.

8. Prediction of 30'x30' Mean Residual Anomalies

Table 8.1 lists the prediction of 32 30' anomalies, in sets of 8 anomalies, in the area bounded by latitudes 8° to 12° S. and longitudes 186° to 188° E. Analogously to the data selection criterion for predicting 1° anomalies, we choose the extent of data for predicting 30' anomalies as $\psi = 0.5$, with density of $\ddot{\rho}$ data grid as 0.2 x 0.3 ($\Delta\lambda \times \Delta\phi$). The data is selected individually for each anomaly, symmetrically around a point down the arc from the center of anomaly block at a distance equal to one-half the separation between the satellites. The results in Table 8.1 are for $\sigma_p = 0.05$ m/s.

For 32 predicted anomalies, the RMS values for the input $\Delta g'$, predicted $\hat{\Delta g}'$, and the prediction discrepancy ϵ are 12.2, 10.5 and 7.3 respectively. Again, the nominal estimate of the standard deviation of 18.1 mgals is pessimistic by a factor of about 2.5. The input and the predicted anomalies have been plotted in Figure 8.1 along four longitudinal profiles. The input anomalies have been joined by full lines and the predicted anomalies by dashed lines. It is clear that the trend of input 30' anomalies is quite faithfully followed by the predicted anomalies. In this area of comparatively smooth anomaly field (also see Fig. 3.2), we generally have a resolution of 30' anomalies but it is perhaps more indicative of satisfactory modeling of the "process" and the "observational" noise.

The average run time for the prediction of a 30' x 30' mean anomaly with the specified data grid selection was only 7 seconds on Amdahl 470 computer. This time could be reduced further if the covariances were approximated by interpolation from stored tables, instead of being computed rigorously.

Table 8.1 Prediction of Mean 30'x 30' Residual Anomalies in Area 8° to 12° S., 186° to 188° E.

Extent of $\hat{\rho}$ Data $\psi = 0.5$;

Density of Data 0.2×0.3 ;

$\sigma_{\hat{\rho}} = 0.05 \text{ mgals}$, $\sigma_{\hat{\rho}} = 1 \mu\text{m/s}$

seq #	Center of Anom. Block		Prediction of Anomaly (mgals)				Statistics for ϵ (mgals)	Correln. Coeff. r
	ϕ_c°	λ_c°	$\Delta g'$	$\hat{\Delta g}'$	ϵ	$\hat{\sigma}_{\Delta g}'$		
1	-8.25	186.25	-15	-10	5	18.0	Min. 2 Max. 13 Mean 6.7	0.69
2	-8.75	"	-19	-7	13	18.1		
3	-9.25	"	-6	3	9	"		
4	-9.75	"	7	9	2	18.0		
5	-10.25	"	5	11	6	18.1		
6	-10.75	"	-2	4	6	"		
7	-11.25	"	-10	-1	9	"		
8	-11.75	"	-6	-1	5	"		
		RMS	10.2	6.9	7.4			
		Mean	-5.7	1.0	6.7	18.1		
9	-8.25	186.75	-13	-8	5	18.2	Min. -1 Max. 17 Mean 6.7	0.80
10	-8.75	"	3	2	-1	18.0		
11	-9.25	"	10	13	3	"		
12	-9.75	"	12	18	6	"		
13	-10.25	"	9	17	8	"		
14	-10.75	"	3	10	7	"		
15	-11.25	"	-10	-1	9	18.2		
16	-11.75	"	-30	-13	17	"		
		RMS	13.8	12.0	8.4			
		Mean	-1.9	4.8	6.7	18.1		
17	-8.25	187.25	-7	-8	0	18.0	Min. -9 Max. 12 Mean -0.2	0.89
18	-8.75	"	13	5	-9	18.1		
19	-9.25	"	20	15	-5	"		
20	-9.75	"	23	19	-4	18.0		
21	-10.25	"	17	18	1	18.1		
22	-10.75	"	0	12	12	"		
23	-11.25	"	-13	-4	10	"		
24	-11.75	"	-12	-17	-5	"		
		RMS	14.9	13.4	6.9			
		Mean	5.1	4.9	-0.2	18.1		
25	-8.25	187.75	-8	-8	0	18.2	Min. -9 Max. 14 Mean -0.3	0.71
26	-8.75	"	-1	-1	0	18.0		
27	-9.25	"	4	5	1	"		
28	-9.75	"	-5	9	14	"		
29	-10.25	"	11	12	1	"		
30	-10.75	"	16	12	-4	"		
31	-11.25	"	13	3	-9	18.2		
32	-11.75	"	-1	-7	-6	"		
		RMS	8.9	8.1	6.5			
		Mean	3.5	3.3	-0.3	18.1		
For all 32 anom.		RMS	12.2	10.5	7.3			
		Mean				18.1		0.80

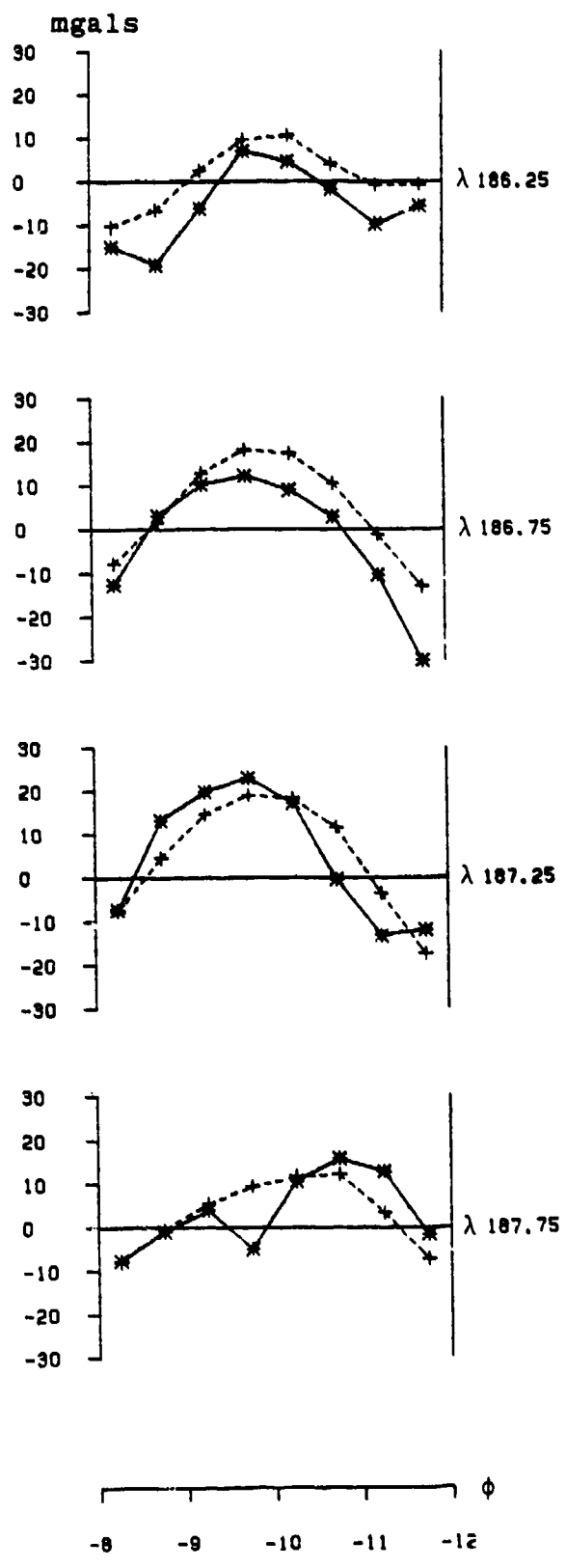


Figure 8.1 Prediction of 30'x 30' Mean Residual Anomalies (mgals). $\sigma_p = 0.05$ mgals; $\sigma_\phi = 1$ um/s. Input anomalies used for simulating ϕ data joined by full lines. Predicted anomalies joined by dashed lines. Extent of data $\psi = 0^\circ 5$; Density of data $0^\circ 2 \times 0^\circ 3$

9. Prediction of 2°x2° Mean Residual Anomalies

To further confirm that large prediction discrepancies for 1° anomalies near, and in the trench area are due to the rapid variation in the anomaly gradient and not due to the resolution limit of the block size, we examine the prediction of 2°x2° mean anomalies. The 2° residual anomalies implied by the 30' residual anomalies (equation (6.1)) are shown in Figure 9.1, and the gradient of this anomaly field is shown in Figure 9.2 at a contour interval of 5 mgals. If we compare Figure 9.2 with the $\ddot{\rho}$ accelerations in Figure 5.5, it is immediately apparent that much greater resolution is possible from the accelerations than can be depicted by 2° anomaly field (cf Fig. 6.2 and 3.2 for 1° and 30' anomaly fields).

Secondly, we notice from Figure 9.2 that the outline of trench from 14° S. proceeding south along 187°5 E. has been considerably generalized due to the coarseness of the resolution of 2° blocks for depicting this short wavelength feature. The variation in anomaly gradient has become the more important feature affecting three 2° blocks centered at 17° S., 185° E.; 17° S., 187° E. and 15° S., 187° E. These blocks would have large prediction discrepancy because of the rapid variation in anomaly gradient.

We in fact find this to be so. Figure 9.3 shows the plot of "true" and predicted anomalies and Table 9.2 lists the prediction of 15 2° anomalies in the area bounded by latitudes 8° to 18° S. and longitudes 184° to 190° E. The extent of data was $\psi = 1^\circ$ for each individual anomaly symmetrically around a point as in Figure 5.3b, with data grid 0:4° x 0:4 , and the results are quoted for $\sigma_{\ddot{\rho}} = 0.05$ mgals.

If we omit all 2° blocks south of latitude 14° S. from consideration due to large variations in anomaly gradients, the RMS value of "true" $\Delta g'$, predicted $\Delta g'$, and prediction discrepancy for 9 anomalies is 6.1, 6.6, 5.3 respectively. Perhaps a larger value of ψ , say 2°, would have resulted in better prediction.

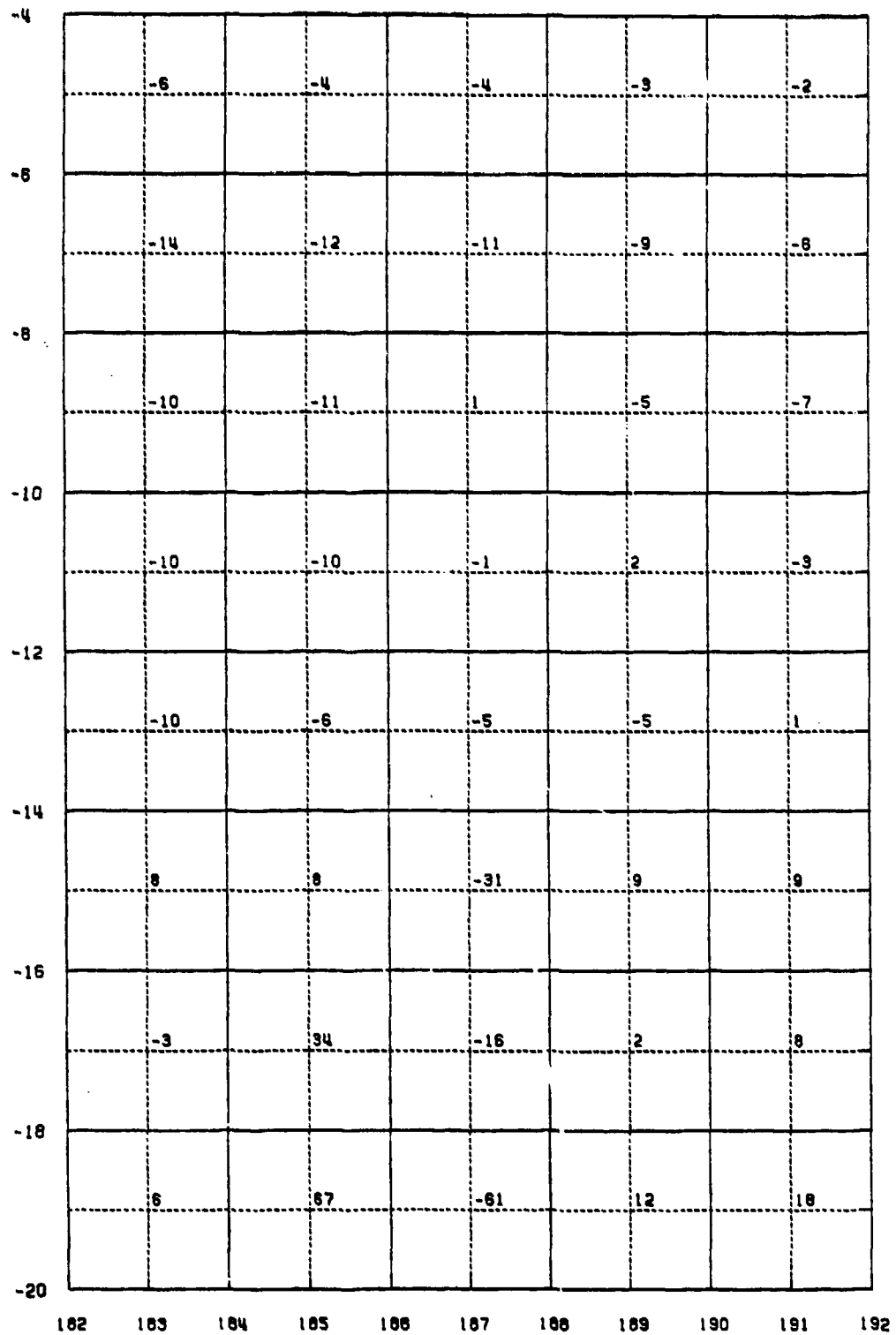


Figure 9.1 2°x2° Mean Residual (to GEM9) Anomalies in mgals. These anomalies are obtained from 30'x30' anomalies in Figure 3.1

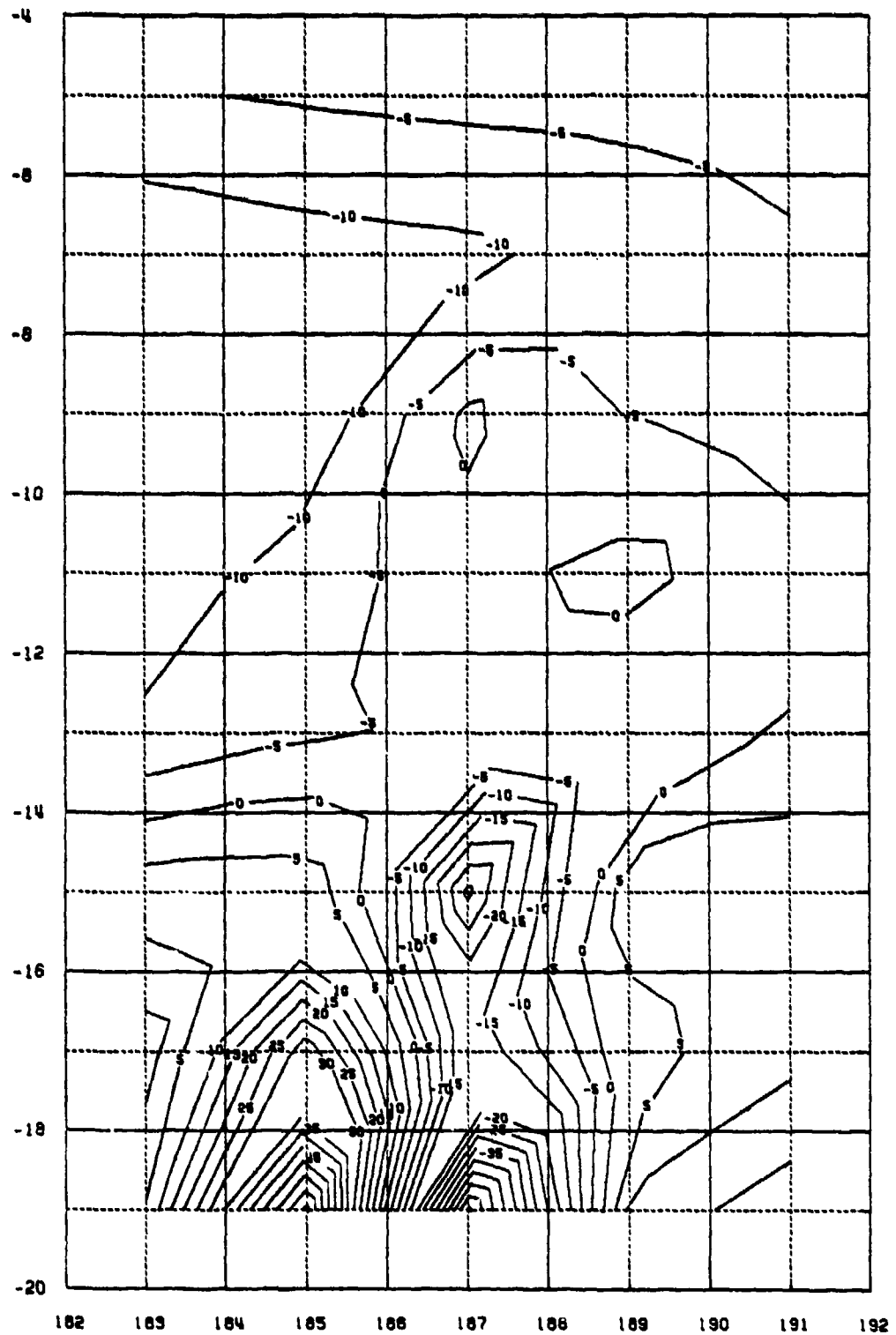


Figure 9.2 Gradient of the 2°x2° Mean Residual (to GEM9) Anomalies. Contour Interval 5 mgals.

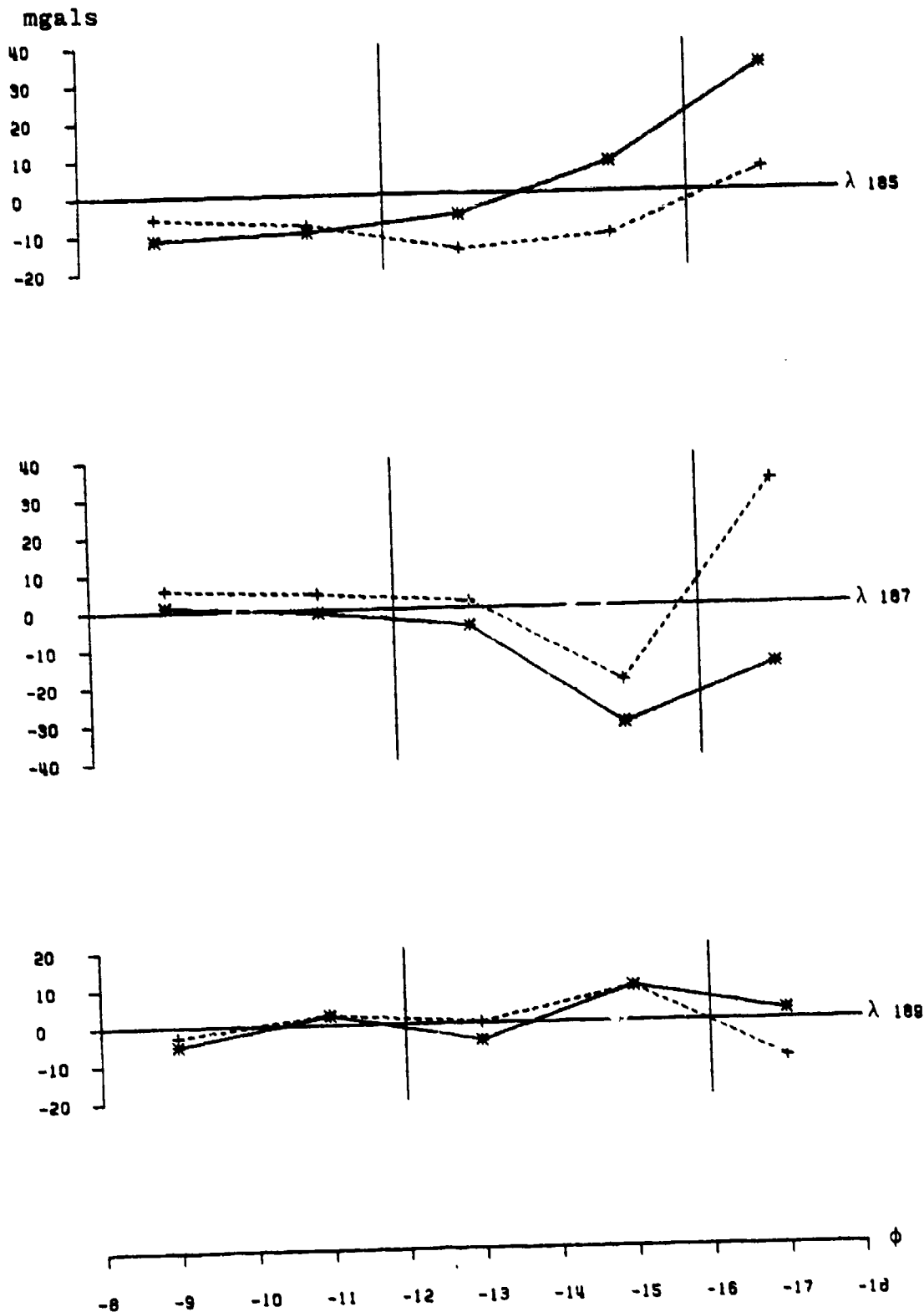


Figure 9.3 Prediction of $2^{\circ} \times 2^{\circ}$ Mean Residual Anomalies (mgals).
 $\sigma_B = 0.05$ mgals; $\sigma_{\phi} = 1$ m/s. "True" anomalies (implied by $30'$
 anomalies used for simulating ϕ data) joined by full lines.
 Predicted anomalies joined by dashed lines. Extent of data
 $\psi = 1^{\circ}$; Density of data 0.4×0.4

Table 9.1 Prediction of Mean 2°x 2° Residual Anomalies in
 Area 8° to 18° S., 184° to 190° E.
 Extent of β Data $\psi = 1^\circ$;
 Density of Data 0.4 x 0.4 ;
 $\sigma_\beta = 0.05$ mgals , $\sigma_\beta = 1\mu\text{m/s}$

seq #	Center of Anom. Block		Prediction of Anomaly (mgals)				Statistics for ϵ (mgals)	Correln. Coeff. r
	ϕ_c°	λ_c°	$\Delta g'$	$\hat{\Delta g}'$	ϵ	$\hat{\sigma}_{\Delta g}'$		
1	-9	185	-11	-6	6	8.6	Min. 0 Max. 6 Mean 3.2	0.83
2	-11	"	-10	-8	2	"		
3	-9	187	1	6	5	"		
4	-11	"	-1	4	5	"		
5	-9	189	-5	-3	2	"		
6	-11	"	2	2	0	"		
RMS			6.6	5.2	3.7			
Mean			-3.9	-0.7	3.2	8.6		
1	-13	185	-6	-15	-9	8.9	Min. -19 Max. 11 Mean -1.0	0.69
2	-15	"	8	-11	-19	8.6		
3	-13	187	-5	2	7	8.5		
4	-15	"	-31	-20	11	8.6		
5	-13	189	-5	0	5	8.9		
6	-15	"	9	9	0	8.6		
RMS			14.2	11.8	10.4			
Mean			-4.8	-5.8	-1.0	8.7		
1	-17	185	34	6	-28	8.7	Min. -28 Max. 49 Mean 2.8	-0.26
2	"	187	-16	33	49	8.5		
3	"	189	2	-10	-12	8.7		
RMS			21.6	20.2	33.2			
Mean			6.9	9.7	2.8	8.6		

10. Summary and Conclusions

The purpose of this simulation study was to test the accuracy of prediction of mean gravity anomalies from the GRAVSAT mission, to establish the resolution achievable in terms of anomaly block size, and to draw conclusions for the data requirement for economical processing in terms of computer time.

Two low satellites were considered in identical nominally polar orbits in a purely gravitational field at an altitude of 150 km over a spherical earth, and with an along-track separation of 200 km between the satellites. The input gravitational field was described by 1500 (residual) 30'x 30' altimeter derived anomalies (R.H. Rapp, private communication, 1980), from which the anomaly implied by the gravitational model GEM9 had been subtracted out. The anomalies covered the area 0° to 25° S. in latitude, and 180° to 195° E. in longitude in the south-west Pacific Ocean, including the sharply varying anomaly field associated with the Tonga Kermedec trench, which lay in the center of the area proceeding in a generally southerly direction from about 14° S.

23,128 range-rate ($\dot{\rho}$) measurements were simulated by Wong and Sjogren (1980) with data interval of 2 seconds, (i.e. $\Delta\phi = 0:14$) and the separation of north to south, as well as south to north, arcs each being 0:2 in longitude (i.e. $\Delta\lambda = 0:2$). This corresponds to a mission duration of 109.4 days (Jekeli and Rapp, 1980, p.12), or a little less than 4 months.

The $\dot{\rho}$ measurements were impressed with a random "observational" noise of mean 0 and standard deviation $1\mu\text{m/s}$ to simulate the precision of the GRAVSAT mission, and supplied to us for this study. The "observations" correspond to residual range-rate, i.e. range-rate observed in the earth's gravitational field minus the computed range-rate in GEM9.

The "noisy" residual range-rate $\dot{\rho}$ was filtered of the observational noise by approximating $\dot{\rho}$ in the least squares sense by a cubic spline function $\dot{\rho}_s$ with fixed knots. It was determined from numerical tests that a spline knot spacing of 10 seconds filtered out a noise, whose RMS value varied from 0.92 to 1.04 $\mu\text{m/s}$ for various arcs. The first derivative of the "smoothed" $\dot{\rho}_s$ was obtained analytically from the spline function, providing us the residual line of sight acceleration, $\ddot{\rho}$ (see equations 2.4 and 2.5).

$\ddot{\rho}$ values were used in this study as the "observations", as these could be easily related to the anomalous potential at the satellite locations. Further, the procedure of obtaining

Court page
49

$\hat{\rho}$ from noisy ρ measurements also largely filters out any systematic errors causing long wavelength perturbations e.g., due to uncertainties in the determination of initial state vectors of the satellites (see page 21).

The residual anomalies $\hat{\Delta g}'$ were predicted in block sizes of $30' \times 30'$, $1^\circ \times 1^\circ$, $2^\circ \times 2^\circ$ using least squares collocation, as in equation 2.9:

$$\hat{\Delta g}' = \underline{A} \underline{T}_\ell ; \underline{A} = \underline{C}_{\Delta g' T_\ell}^T \underline{C}^{*-1} ; \underline{C}^* = \underline{C}_{T_\ell T_\ell} + \underline{D}$$

where $\underline{T}_\ell \equiv \hat{\rho}$ is the "observational" data used in the prediction, with the associated noise matrix \underline{D} . $\underline{C}_{T_\ell T_\ell}$ is the auto-covariance matrix of the $\hat{\rho}$ data, while $\underline{C}_{\Delta g' T_\ell}$ is its cross-covariance vector with the residual anomaly of specified block size. \underline{A} may be called the estimating operator or weight function (see Fig. 5.6, p.26), which may be examined to judge if distant data may be excluded without significantly affecting the predicted value. The underlying covariance functions $\underline{C}_{T_\ell T_\ell}$ and $\underline{C}_{\Delta g' T_\ell}$ may also be examined for their correlation distance (see Fig. 5.1, 5.2, pp. 17, 19).

It was inferred from these considerations that for predicting residual $1^\circ \times 1^\circ$ mean anomalies (residual to GEM9, complete to degree and order 20), a data cap of spherical radius 1° is adequate. More distant data not only contribute to the prediction with decreasing amplitude, but also with varying sign tending to largely cancel out the contribution. Further, there is no improvement in the predicted value of 1° residual anomalies if density of data is increased beyond 0.4×0.4 , which is about one-third of the correlation distance of $\underline{C}_{\Delta g' T_\ell}$. These conclusions were borne out by numerical tests in Tables 6.1 and 6.2 by examining the prediction discrepancy ϵ in equation 5.1:

$$\epsilon = \hat{\Delta g}' - \Delta g'$$

where $\hat{\Delta g}'$ is the predicted value and $\Delta g'$ is the input, or the implied residual anomaly obtained by meaning the input $30'$ residual anomalies used for simulating $\hat{\rho}$ measurements.

This leads to a very modest data requirement for predicting 1° anomalies, i.e. a data density of about 0.4×0.4 in a data cap of spherical radius 1° , a total of about 20 data points. The needed density would be available in a GRAVSAT mission of about one month. Longer duration of mission would permit detection of systematic errors and editing of data of doubtful quality

Several 1° anomalies may be predicted in a single run, separately selecting data symmetrically for each individual anomaly. The average time for predicting each 1° anomaly was about 12 seconds on Amdahl 470 V/6-II computer. In this study, the covariances were rigorously computed necessitating 16 calls to COVAX (Tscherning, 1976) for computing each element of $C_{T_1 T_2}$, and similar lengthy computations for $C_{\Delta g' T_2}$. The time for prediction of each 1° anomaly could be substantially reduced, by interpolating covariances from stored tables.

It was noted from Fig. 5.2 and 5.6 for $C_{\Delta g' T_2}$ and the estimating operator A that the data cap should be centered not at the center of anomaly block being predicted, but at a distance from the block center down the arc equal to one-half the separation between the satellites. This is also shown in Fig. 5.3b (page 20).

Rummel (1980, p.13) had related $\sigma_{\ddot{\rho}}$, the noise of $\ddot{\rho}$ as 0.05 mgals corresponding to the noise of $\dot{\rho}$ of $1\mu\text{m/s}$ at satellite altitude of 150 km. This was numerically confirmed in this study by examining the estimating operator A (p.26) for different values of $\sigma_{\ddot{\rho}}$. For smaller values than 0.05 mgals, the oscillations of A were with much greater amplitude resulting from unstable inversion of $C_{T_1 T_2}$. On the other hand, for values of $\sigma_{\ddot{\rho}}$ larger than 0.05 mgals, the oscillations of A were damped out.

24 $1^\circ \times 1^\circ$ residual anomalies were predicted in the area 8° to 12° S. latitude and 184° to 190° E. longitude, which was near but away from the trench, and thus with a comparatively smooth anomaly gradient field (p.29). The RMS prediction discrepancy for the 24 anomalies was 5.5 mgals, while the RMS value of "true" anomalies was 9.5 mgals. The correlation coefficient between the predicted and true anomalies was 0.84 (see page 34).

This showed a good agreement for "smooth" anomaly gradient field. The prediction of 1° anomalies was then tried in the "rough" anomaly gradient field while approaching, and then directly over the trench. This was done in latitude 12° - 18° S. along two longitudinal profiles of $186^\circ 5'$ and $187^\circ 5'$ E. The first profile was immediately to the west of the trench, while the second profile was directly over the trench. It was found (page 36) that though the "high" and "low" in the anomaly field were generally predicted satisfactorily, the intervening anomalies were smoothed out between the extreme values. Further, the prediction was poor whenever the sign of anomaly gradient changed; and particularly over the trench, the very rapid short wavelength variations in the anomaly gradient were practically sensed as zero at the satellite altitude. This is also seen in the plot of accelerations, $\ddot{\rho}$, sensed at the satellite (see page 25).

The question of the resolution achievable in terms of anomaly block size was addressed by predicting 32 residual 30'x30' anomalies in the smooth anomaly gradient field in the area 8° to 12° S. latitude and 186° to 188° E. longitude. The RMS prediction discrepancy for the 32 anomalies was 7.3 mgals, while the RMS value of "true" anomalies was 12.2 mgals (see page 38). The plot of predicted and true (i.e. input) 30' anomalies shows (see page 39) that while the general trend of 30' anomalies was faithfully predicted, the individual short wavelength feature in 30' anomalies were not correctly predicted particularly when the sign of anomaly gradient changed sharply.

The problem of prediction when anomaly gradients are changing sharply was again found while predicting 2°x2° anomalies in the area 8° to 18° S. in latitude, and 184° to 190° E. in longitude (page 44). 9 residual 2° anomalies between 8° to 14° S. latitude had a RMS prediction discrepancy of 5.3 mgals, while the RMS value of true anomalies was 6.1 mgals. The prediction in the sharply varying anomaly gradient field south of 14° S. was unsatisfactory (page 42). It was however clear that there was considerably more detail in the accelerations sensed at the satellite (page 25) compared to the variations which may be represented in the 2° anomaly field (page 42).

It was also found that the formal estimate of the standard deviation of the prediction (equation 2.10) was 2.3 to 2.5 times larger than the RMS prediction discrepancy. This was due to the use of a global covariance function (Tscherning and Rapp, 1974) instead of a local covariance function, which may have permitted a better fit to the variance of anomaly gradients in the area. This parallels the conclusion of Schwarz and Lachapelle (1980), who found the estimate of standard deviation of the prediction from the global covariance function to be about three times larger in Canada.

We may conclude that this simulation study has established satisfactory procedures for predicting the anomalous gravitational field from the range-rate data from GRAVSAT mission. It has also established the requirement of data for economical processing in terms of computer time. The resolution achievable is 1°x1° anomaly blocks with an accuracy of prediction of about 5.5 mgals. But this is possible only in areas where the anomaly gradients are not varying sharply, e.g. areas associated with trenches. Near the trench, the anomaly highs and lows may be predicted satisfactorily, but the intervening anomalies would be smoothed out between the extreme values. However, directly over the trench, the prediction from range rate data at satellite altitude would be unsatisfactory due to the very rapid short-wavelength variations in the anomaly gradients, which is not resolved at the satellite altitude.

It was found in this study that though the estimates of the formal standard deviation of the predicted 1° anomalies were reduced with the increase in size of the data cap, and with the increase in the density of data inside the cap, there was little improvement in the predicted value of 1° anomalies by least squares collocation technique. Besides, there was a large increase in the computer time required for the processing of the increased data. Further studies are required to determine if other techniques, or a modification of least squares collocation technique, would allow the economical processing of increased data. And, if the use of the increased data would, in addition to lowering the estimate of the standard deviation, also result in significant improvement of the predicted value of the anomalies.

References

- Bergeson-Willis, S.E., D.E. Smith and V.L. Pisacane, The Current (1981) Dedicated Gravitational Satellite Mission, Preprint for Presentation at XXXII International Astronautical Federation Congress, Rome, Sept. 1981.
- Breakwell, J.V., More About Satellite Determination of Short Wavelength Gravity Variations, Dept. of Aeronautics and Astronautics, Stanford Univ., California, Apr. 1980.
- Breakwell, J.V. and T. Duhamel, The Weighting of Nearby Satellite Data in Estimating Local Gravity, Dept. of Aeronautics and Astronautics, Stanford Univ., California, May 1981.
- Douglas, B.C., C.C. Goad and F.F. Morrison, Determination of the Geopotential from Satellite to Satellite Tracking Data, J. Geophys. Res., Vol. 85, No. B10, pp. 5471-5480, Oct. 1980.
- Hajela, D.P., Recovery of 5° Mean Gravity Anomalies in Local Areas from ATS-6/Geos3 Satellite to Satellite Range Rate Observations, Dept. of Geodetic Science Report No. 259, The Ohio State Univ., Columbus, Sept. 1977.
- Hajela, D.P., Tests for the Recovery of 5° Mean Gravity Anomalies in Local Areas from ATS-6/Geos3 Satellite to Satellite Range Rate Observations, J. Geophys. Res., Vol. 84, No. B12, pp. 6884-6890, Nov. 1979.
- Heiskanen, W.A. and H. Moritz, Physical Geodesy, W.H. Freeman, San Francisco, 1967.
- Jekeli, C. and R.H. Rapp, Accuracy of the Determination of Mean Anomalies and Mean Geoid Undulations from a Satellite Gravity Field Mapping Mission, Dept. of Geodetic Science Report No. 307, The Ohio State Univ., Columbus, Aug. 1980.
- Krynski, J., Improvement of the Geoid in Local Areas by Satellite to Satellite Tracking, Bulletin Geodesique, Vol. 53, No. 1, pp. 19-36, 1979.
- Lancaster, E.R., R.H. Estes and D.C. Chin, Gravsat Error Analysis Results for One Degree Gravity Resolution, NASA Document X-932-80-2, Goddard Space Flight Center, Greenbelt, Maryland, Jan. 1980.
- Lerch, F.J., S.M. Klosko, R.E. Laubscher and C.A. Wagner, Gravity Model Improvement Using Geos 3 (GEM9 and 10), J. Geophys. Res., Vol. 84, No. B8, pp. 3897-3916, July 1979.
- Moritz, H., Advanced Physical Geodesy, Abacus Press, 1980.

- National Academy of Sciences, Application of a Dedicated Gravitational Satellite Mission, Report of the Panel on Gravity Field and Sea Level of the Committee on Geodesy, Washington, D.C., 1979.
- Pisacane, V.L. and S.M. Yionoulis, Recovery of Gravity Variations from Satellite to Satellite Tracking, Applied Physics Laboratory Rep. SD05583, The Johns Hopkins Univ., Laurel, Maryland, Apr. 1980.
- Rapp, R.H. and D.P. Hajela, Accuracy Estimates of $1^\circ \times 1^\circ$ Mean Anomaly Determination from a High-Low SST Mission, Dept. of Geodetic Science Report No. 295, The Ohio State Univ., Columbus, Sept. 1979.
- Rummel, R., Geoid Heights, Geoid Height Differences, and Mean Gravity Anomalies from "Low-Low" Satellite to Satellite Tracking - An Error Analysis, Dept. of Geodetic Science Report No. 309, The Ohio State Univ., Columbus, June 1980.
- Rummel, R., D.P. Hajela and R.H. Rapp, Recovery of Mean Gravity Anomalies from Satellite to Satellite Range Rate Data Using Least Squares Collocation, Dept. of Geodetic Science Report No. 248, The Ohio State Univ., Columbus, Sept. 1976.
- Rummel, R., K.P. Schwarz and M. Gerstl, Least Squares Collocation and Regularisation, Bulletin Geodesique, Vol. 53, No. 4, pp. 343-361, 1979.
- Schwarz, K.P., Geodetic Accuracies Obtainable from Measurements of First and Second Order Gravitational Gradients, Dept. of Geodetic Science Report No. 242, The Ohio State Univ., Columbus, Aug. 1976.
- Schwarz, K.P. and G. Lachapelle, Local Characteristics of the Gravity Anomaly Covariance Function, Bulletin Geodesique, Vol. 54, No. 1, pp. 21-36, 1980.
- Sünkel, H., A Covariance Approximation Procedure, Dept. of Geodetic Science Report No. 286, The Ohio State Univ., Columbus, March 1979.
- Sünkel, H., Cardinal Interpolation, Dept. of Geodetic Science Report No. 312, The Ohio State Univ., Columbus, March 1981.
- Tscherning, C.C., Covariance Expressions for Second and Lower Order Derivatives of the Anomalous Potential, Dept. of Geodetic Science Report No. 225, The Ohio State Univ., Columbus, Jan. 1976.
- Tscherning, C.C. and R.H. Rapp, Closed Covariance Expressions for Gravity Anomalies, Geoid Undulations and Deflections of the Vertical Implied by Anomaly Degree Variance Models, Dept. of Geodetic Science Report No. 208, The Ohio State Univ., Columbus, May 1974.

Wong, L. and W.L. Sjogren, Simulation of Gravity Anomaly
Recovery From Satellite to Satellite Tracking Data,
June, 1980.